

Accelerating Large-Scale Regularized High-Order Tensor Recovery

Wenjin Qin, Hailin Wang, *Student Member, IEEE*, Jingyao Hou, Jianjun Wang, *Member, IEEE*

Abstract—Currently, existing tensor recovery methods fail to recognize the impact of tensor scale variations on their structural characteristics. Furthermore, existing studies face prohibitive computational costs when dealing with large-scale high-order tensor data. To alleviate these issues, assisted by the Krylov subspace iteration, block Lanczos bidiagonalization process, and random projection strategies, this article first devises two fast and accurate randomized algorithms for *low-rank tensor approximation* (LRTA) problem. Theoretical bounds on the accuracy of the approximation error estimate are established. Next, we develop a novel generalized nonconvex modeling framework tailored to large-scale tensor recovery, in which a new regularization paradigm is exploited to achieve insightful prior representation for large-scale tensors. On the basis of the above, we further investigate new unified nonconvex models and efficient optimization algorithms, respectively, for several typical high-order tensor recovery tasks in unquantized and quantized situations. To render the proposed algorithms practical and efficient for large-scale tensor data, the proposed randomized LRTA schemes are integrated into their central and time-intensive computations. Finally, we conduct extensive experiments on various large-scale tensors, whose results demonstrate the practicability, effectiveness and superiority of the proposed method in comparison with some state-of-the-art approaches.

Index Terms—Tensor recovery, tensor approximation, quantized observation, block Lanczos bidiagonalization, randomized projection, nonconvex regularization, gradient tensor modeling.

I. INTRODUCTION

THE era of “Big Data” has witnessed massive amounts of multi-dimensional, multi-modal datasets in numerous modern applications, which are characterized by (i) large Volume, (ii) high Velocity, and (iii) high Veracity, and (iv) high Variety [1], [2]. Each of the “V” features represents a research challenge in its own right. For instance, large Volume demands scalable strategies that can adapt to increasing data scales; high Velocity requires high-efficiency processing mechanisms to ensure timely analysis; high Veracity calls for robust and reliable methods for noisy, incomplete and/or inconsistent data. As such, developing innovative solutions and technologies to

process and analyze big data within an acceptable timeframe has become increasingly urgent and crucial.

Tensors possess the capability to represent a wide range of big data with multi-dimensional/modal/relational/view characteristics. Compared with vector/matrix structure-based representations, tensor can more faithfully and accurately capture essential structures and correlations underlying complex big data. Thus, tensor-based approaches and theories have been developed for data processing and analysis in recent years [3], [4]. Among them, tensor recovery is the most fundamental and crucial task, which addresses the challenge of reconstructing the original tensor from its imperfect counterpart degraded by noise/outliers corruption, information loss, and other factors [5]–[16]. This research topic has increasingly drawn significant attention across various domains, such as statistics [5], medicine [17], transportation [18], wireless communications [19], remote sensing [20], machine learning [7], signal/image processing [16], [21], and computer vision [22].

From the modeling perspective, tensor recovery covers *Low-Rank Tensor Completion* (LRTC) [23]–[32], *Robust LRTC* (RLRTC) [33]–[42], *Tensor Robust Principal Component Analysis* (TRPCA) [10], [11], [14], [30], [43]–[46], and *Tensor Compressive Sensing* [12], [13], [47]–[49]. Based on the solutions and techniques employed, these studies can be further subdivided into two branches. The first branch is factorization-based methods, which alternatively update the factors with the predefined initial tensor rank. Existing classical studies are developed via alternating least squares [25]–[27], [35], variational Bayesian inference [23], [24], [43], gradient-oriented optimization approach [6]–[9], [49], etc. The other important branch is regularization-based methods, which focuses more on characterizing prior structures (e.g., low-rankness and sparsity priors) underlying tensor data finely via proper regularization items. Some typical convex regularizers include SNN [33] under Tucker framework, TRNN [28], [34] under *tensor ring* (TR) framework, FCTN nuclear norm [36] under *Fully-Connected Tensor Network* (FCTN) framework, and HTNN [29], WSTNN [30], METNN [31], TCTV [14] under *Tensor Singular Value Decomposition* (T-SVD) framework. To further enhance the recovery performance, a series of nonconvex variants have been subsequently proposed [16], [44], [45], [50]–[59].

Although the above regularization-based methods yield commendable performance in practical applications, they demonstrate inefficiency in handling large tensor data. In response to the demands of the big data era, it is of crucial importance to address the issue of large-scale tensor recovery in a fast and accurate manner. Speed is manifested in the computation module, whereas accuracy is embodied in the modeling module. However, achieving high accuracy and high speed simultaneously remains fraught with challenges, because

This work was supported in part by the National Key Research and Development Program of China under Grant 2023YFA1008502; in part by the National Natural Science Foundation of China’s Regional Innovation Development Joint Fund under Grant U24A2001; in part by the Natural Science Foundation of Chongqing, China, under Grant CSTB2023NSCQ-LZX0044; in part by the National Natural Science Foundation of China under Grant 12301594, Grant 12201505, Grant 12101512; in part by the Chongqing Talent Project, China, under Grant cstc2021ycjh-bgzxm0015; in part by the Fundamental Research Funds for the Central Universities under Grant SWU-KR25013; and in part by the Initiative Projects for Ph.D. in China West Normal University under Grant 22ke030. (Corresponding author: Jianjun Wang.)

Wenjin Qin and Jianjun Wang are with the School of Mathematics and Statistics, Southwest University, Chongqing 400715, China (e-mail: qinwenjin2021@163.com, wjj@swu.edu.cn). Hailin Wang is with the School of Mathematics and Statistics, Xi’an Jiaotong University, Xi’an 710049, China (e-mail: wanghailin97@163.com). Jingyao Hou is with the School of Mathematics and Information, China West Normal University, Nanchong 637009, China (e-mail: hjy17623226280@163.com).

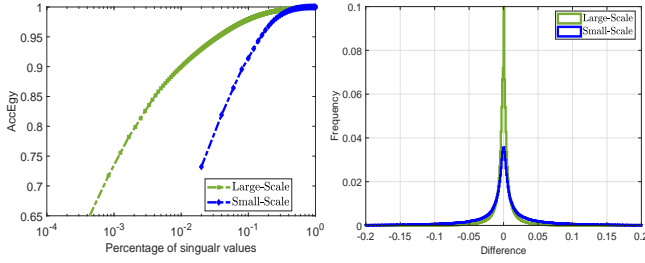


Fig. 1: An illustration of the distinctions in \mathbf{L} and \mathbf{S} prior structures between small-scale and large-scale tensors. **Top:** The AccEgy ($AccEgy = \sum_{i=1}^k \sigma_i^2 / \sum_{j=1}^2 \sigma_j^2$ with σ_i denotes the i -th tensor singular value) versus the percentage of singular values; **Right:** Frequency histograms of all corresponding elements of gradient tensor.

there is a trade-off between accuracy and speed.

One of the challenges lies in how to explore effective and concise regularization strategies to reveal the insightful prior features of large-scale high-order tensors, and further investigate reliable and scalable recovery models. Previous studies (e.g., [14], [16], [29]–[32], [53]) have not managed to cast deep insights upon the prior information of large high-order tensors. Besides, they are still in a state of unawareness regarding the ramifications of tensor scale fluctuations on their structural characteristics. As illustrated in Figure 1, we uncover a universal phenomenon: with the increase in the scale of tensor data, it tends to simultaneously exhibit stronger global low-rankness (\mathbf{L}) and local smoothness (\mathbf{S}). To profoundly excavate these two crucial prior structures, we consider exploring a novel regularization strategy, in which generalized nonconvex constraints are imposed on the resulting gradient maps of the original big tensors. Different from the nonconvex low-rank regularization methods that previously acted on the original domain [16], [44], [45], [50]–[59], this gradient mapping-based nonconvex paradigm can simultaneously encode $\mathbf{L}+\mathbf{S}$ priors in a concise manner, and demonstrates superiority and effectiveness. A supporting example shown on the right-hand side of Figure 2 indicates that in the same scenario, as the scale of tensor data expands, the performance of tensor recovery methods becomes increasingly prominent. Moreover, the performance disparity between the proposed nonconvex GNHTC method based on the joint \mathbf{L} and \mathbf{S} priors and the others only utilizing the \mathbf{L} prior also becomes more pronounced.

From a computational perspective, existing tensor recovery methods generally require to perform the SVD-based (e.g., [14], [16], [28]–[34], [44], [45], [50]–[59]) or alternating minimization-based (e.g., [25]–[27], [35], [36]) multiple low-rank approximations. These studies suffer from the curse of dimensionality when dealing with large-scale high-order tensor data, thereby leading to high computational costs and storage requirements. As illustrated on the left-side of Figure 1, with the escalation of the scale of tensor data, it typically manifests a heightened degree of redundancy, which is tantamount to the low-rank property. As thus, another challenge lies in how to develop efficient low-rank compression and approximation methods for large-scale tensors, with the aim of achieving dimension-reduction and elevating computational efficiency.

Randomized sketching approach is a powerful tool for

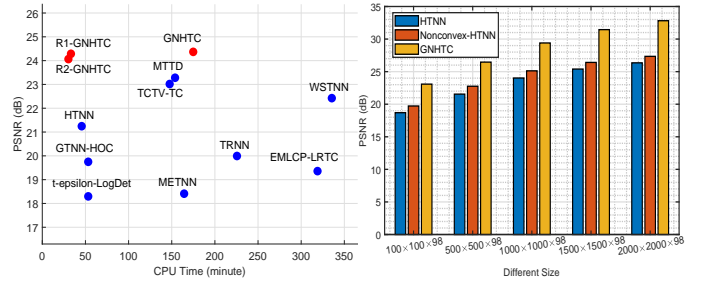


Fig. 2: **Left:** The CPU time versus average PSNR in LRTC task (see Table II for more details). The proposed randomized algorithms achieve the lowest computation cost. **Right:** The tensor scale versus average PSNR in LRTC task.

handling optimization problems involving a large amount of data, which is known for its low memory and computational complexities (e.g., [2], [60]–[68]). Driven by these advantages, several popular sketching techniques (e.g., random sampling [69]–[72], random projection [73]–[79], coresets [80]) have been employed to design fast randomized low-rank approximation algorithms for large-scale tensors. However, existing approximation algorithms based on T-SVD essentially perform dimensionality reduction on the spatial modes [16], [72]–[74], thereby resulting in suboptimal computational efficiency. To tackle the aforementioned concerns, we consider designing efficient and adaptive Tucker compression methods, which executes dimensionality reduction along each mode of the tensor, as a preprocessing step. Following this preprocessing, the associated deterministic algorithms under T-SVD framework can be quickly computed via the smaller Tucker core tensor.

On the basis of the two research contents considered above, we continue to think about how to develop robust, scalable, and reliable algorithms equipped with convergence guarantee to solve the formulate tensor recovery models that leverages generalized nonconvex regularizers. In addition, our consideration also involves embedding the developed fast randomized compression and approximation algorithms into the main and time-consuming calculations of the proposed recovery method, thereby enhancing its practicality and efficiency of processing large-scale tensor data. To sum up, in this article, we delve into an innovative generalized nonconvex tensor modeling method, which exhibits powerful capabilities in prior characterization of large-scale high-order tensors. Besides, novel fast randomized *low-rank tensor approximation* (LRTA) algorithms leveraging full-mode random projection strategy are incorporated to alleviate computational bottlenecks encountered when dealing with large-scale tensor data. Main contributions of this work are summarized as follows:

1) Firstly, leveraging the block Krylov subspace approach, block Lanczos bidiagonalization process and random projection technique, we devise efficient randomized algorithms for solving fixed-rank and fixed-precision LRTA problems in the Tucker format, respectively. Theoretical bounds on the accuracy of the approximation error estimate are established. Compared with the deterministic LRTA methods, the proposed one exhibit remarkable advantage in computational efficiency.

2) Secondly, a novel generalized nonconvex tensor modeling framework is developed by investigating new regularization

schemes. The first scheme has a strong ability to encode two insightful and essential tensor prior information simultaneously, i.e., $\mathbf{L}+\mathbf{S}$ priors, and the second scheme can well enhance the robustness against various structured noise/outliers, like entry-wise, slice-wise and tube-wise forms. Notably, the proposed framework includes most existing relevant approaches as special cases.

3) Thirdly, efficient and scalable models, along with their optimization algorithms with convergence guarantees, are investigated for several typical tensor recovery tasks in both unquantized and quantized scenarios. The coupling of the proposed randomized LRTA strategies can significantly quicken the computational speed of the developed recovery algorithms, especially for large-scale high-order tensors (see Figure 2). The practicability, effectiveness and superiority of the proposed method are proven by extensive experiments on various large-scale multi-dimensional data.

What is particularly noteworthy is that all theoretical proofs, related algorithms, and more experimental results of this article are provided in the supplementary material.

II. NOTATIONS AND PRELIMINARIES

In this section, the main notations and preliminaries utilized in the whole paper are summarized, most of which originate from the literatures [14], [16], [29], [81], [82].

We use x , \mathbf{x} , \mathbf{X} , and \mathcal{X} to denote scalars, vectors, matrices, and tensors, respectively. For a matrix $\mathbf{X} \in \mathbb{R}^{m \times n}$, $\mathbf{I}_n \in \mathbb{R}^{n \times n}$, $\text{trace}(\mathbf{X})$, $\mathbf{X}^H(\mathbf{X}^T)$, $\langle \mathbf{X}, \mathbf{Y} \rangle = \text{trace}(\mathbf{X}^H \cdot \mathbf{Y})$ and $\|\mathbf{X}\|_* = (\sum_i |\sigma_i(\mathbf{X})|)$ denote its identity matrix, trace, conjugate transpose (transpose), inner product and nuclear norm, respectively. For an order- d tensor $\mathcal{X} \in \mathbb{R}^{n_1 \times \dots \times n_d}$, $\mathcal{X}_{i_1, \dots, i_d}$ denotes its (i_1, \dots, i_d) -th element, $\mathbf{X}_{(k)}$ denotes its **mode- k unfolding**, and $\mathcal{X}^{<j>} := \mathcal{X}(:, :, i_3, \dots, i_d), j = \sum_{a=4}^d (i_a - 1) \prod_{b=3}^{a-1} n_b + i_3$ is called as its **face slice**. Then $\text{bdiag}(\mathcal{X})$ is the **block diagonal matrix** whose i -th block equals to $\mathcal{X}^{<i>}$, $\forall i \in \{1, 2, \dots, n_3 \dots n_d\}$. The **inner product** of two tensors \mathcal{X} and \mathcal{Y} with the same size is defined as $\langle \mathcal{X}, \mathcal{Y} \rangle = \sum_{j=1}^{n_3 n_4 \dots n_d} \langle \mathcal{X}^{<j>}, \mathcal{Y}^{<j>} \rangle$. The **ℓ_1 -norm**, **Frobenius norm**, **tube $_1$ -norm** and **slice $_1$ -norm** of \mathcal{X} are defined as $\|\mathcal{X}\|_{\ell_1} = (\sum_{i_1, \dots, i_d} |\mathcal{X}_{i_1, \dots, i_d}|)$, $\|\mathcal{X}\|_F = (\sum_{i_1, \dots, i_d} |\mathcal{X}_{i_1, \dots, i_d}|^2)^{\frac{1}{2}}$, $\|\mathcal{X}\|_{\text{tube}_1} = \sum_{i_1, i_2} \|\mathcal{X}_{i_1 i_2 \dots}\|_F$, $\|\mathcal{X}\|_{\text{slice}_1} = \sum_{i_3, \dots, i_d} \|\mathcal{X}(:, :, i_3, \dots, i_d)\|_F$, respectively.

Let $\mathcal{L}(\mathcal{X})$ or $\mathcal{X}_{\mathcal{L}}$ represent the result of invertible linear transforms \mathcal{L} on $\mathcal{X} \in \mathbb{R}^{n_1 \times \dots \times n_d}$, i.e.,

$$\mathcal{L}(\mathcal{X}) = \mathcal{X} \times_3 \mathbf{U}_{n_3} \times_4 \mathbf{U}_{n_4} \dots \times_d \mathbf{U}_{n_d}, \quad (1)$$

where $\mathcal{X} \times_j \mathbf{U}_{n_j}$ denotes the mode- j product of \mathcal{X} with matrix \mathbf{U}_{n_j} , and the transform matrices $\mathbf{U}_{n_i} \in \mathbb{C}^{n_i \times n_i}$ of \mathcal{L} satisfies:

$$\mathbf{U}_{n_i} \cdot \mathbf{U}_{n_i}^H = \mathbf{U}_{n_i}^H \cdot \mathbf{U}_{n_i} = \alpha_i \mathbf{I}_{n_i}, \forall i \in \{3, \dots, d\}, \quad (2)$$

in which $\alpha_i > 0$ is a constant. The inverse operator of $\mathcal{L}(\mathcal{X})$ is defined as $\mathcal{L}^{-1}(\mathcal{X}) = \mathcal{X} \times_d \mathbf{U}_{n_d}^{-1} \times_{d-1} \mathbf{U}_{n_{d-1}}^{-1} \dots \times_3 \mathbf{U}_{n_3}^{-1}$, and $\mathcal{L}^{-1}(\mathcal{L}(\mathcal{X})) = \mathcal{X}$.

Based on the above concepts, we introduce related tensor product, tensor decompositions and ranks utilized in this paper.

Definition II.1. (T-Product [29]) Let $\mathcal{X} \in \mathbb{R}^{n_1 \times n_2 \times n_3 \times \dots \times n_d}$ and $\mathcal{Y} \in \mathbb{R}^{n_2 \times l \times n_3 \times \dots \times n_d}$. Then the invertible linear transforms \mathcal{L} based t-product is defined as

$$\mathcal{C} = \mathcal{X} *_\mathcal{L} \mathcal{Y} = \mathcal{L}^{-1}(\mathcal{L}(\mathcal{X}) \triangle \mathcal{L}(\mathcal{Y})), \quad (3)$$

where \triangle denotes the face-wise product ($\mathcal{P} = \mathcal{M} \triangle \mathcal{N}$ implies $\mathcal{P}^{<j>} = \mathcal{M}^{<j>} \cdot \mathcal{N}^{<j>}$, $j = 1, \dots, n_3 \dots n_d$).

The relevant algebraic basis induced by high-order t-product can be found in the literatures [14], [16], [29], such as identity, orthogonality, inverse, transpose, T-SVD factorization, T-QR factorization, T-SVD rank.

Definition II.2. (T-SVD factorization and rank [29]) Let $\mathcal{X} \in \mathbb{R}^{n_1 \times \dots \times n_d}$, then it can be factorized as

$$\mathcal{X} = \mathcal{U} *_\mathcal{L} \mathcal{S} *_\mathcal{L} \mathcal{V}^T, \quad (4)$$

where $\mathcal{U} \in \mathbb{R}^{n_1 \times n_1 \times n_3 \times \dots \times n_d}$ and $\mathcal{V} \in \mathbb{R}^{n_2 \times n_2 \times n_3 \times \dots \times n_d}$ are orthogonal, $\mathcal{S} \in \mathbb{R}^{n_1 \times n_2 \times n_3 \times \dots \times n_d}$ is a f -diagonal tensor. Then, the T-SVD rank of \mathcal{X} is defined as

$$\text{rank}_{\text{tsvd}}(\mathcal{X}) = \sum_i \mathbb{1}[\mathcal{S}(i, i, :, \dots, :) \neq \mathbf{0}],$$

where $\mathbb{1}[\cdot]$ denotes the indicator function.

Definition II.3. (Tucker factorization and rank [81]) Let $\mathcal{X} \in \mathbb{R}^{n_1 \times \dots \times n_d}$, then its Tucker decomposition form is

$$\mathcal{X} \triangleq [\mathcal{C}; \mathbf{F}_1, \mathbf{F}_2, \dots, \mathbf{F}_d] = \mathcal{C} \times_1 \mathbf{F}_1 \times_2 \mathbf{F}_2 \dots \times_d \mathbf{F}_d, \quad (5)$$

where $\{\mathbf{F}_i\}_{i=1}^d \in \mathbb{R}^{n_i \times r_i}$ are the factor matrices and can be thought of as the principal components along different mode. $\mathcal{C} \in \mathbb{R}^{r_1 \times \dots \times r_d}$ is the core tensor and its entries show the level of interaction between the different components. The vector $\mathbf{r} = (r_1, \dots, r_d)$ is defined as the Tucker-rank of \mathcal{X} , where $r_j = \text{rank}(\mathbf{X}_{(j)})$, $j = 1, \dots, d$.

Proposition II.1. [83] Let x and ξ be two independent random variables, where $|x| < \beta$ holds almost surely and ξ is uniformly distributed on the interval $[-\theta, \theta]$ with $\gamma \geq \beta$. Then we have

$$\mathbb{E}(x) = \mathbb{E}(\theta \cdot \text{sign}(x + \xi)).$$

III. FAST RANDOMIZED HIGH-ORDER TENSOR APPROXIMATION

In this section, fast and accurate randomized algorithms are devised for solving fixed-rank and fixed-precision LRTA problems, respectively. Furthermore, we provide the error bound analysis for these two randomized algorithms. **Due to space limitations, the complexity analysis and experimental results are included in the supplementary materials.**

A. Proposed Randomized LRTA Algorithms

The truncated higher-order SVD (THOSVD) [81] and the sequentially truncated higher-order SVD (STHOSVD) [84] algorithms rely directly on SVD when computing the singular vectors of intermediate matrices. Consequently, they demand significant memory and high computational complexity when the size of tensors is large. To alleviate this issue, Minster et al. [85] designed their corresponding accelerated versions (i.e.,

Algorithm 1: STHOSVD Using Randomized Block Krylov Iteration Method, **R-STHOSVD-BKI**.

Input: $\mathcal{X} \in \mathbb{R}^{n_1 \times \dots \times n_d}$, target rank: $\mathbf{r} = (r_1, \dots, r_d)$, processing order: ρ , block size: $\mathbf{b} = (b_1, \dots, b_d)$, Krylov iterations: $\mathbf{q} = (q_1, \dots, q_d)$, $1 \leq b_i \leq r_i$, $(q_i + 1) \cdot b_i \geq r_i$, $i = 1, 2, \dots, d$.

Output: $\hat{\mathcal{X}} = [\mathcal{C}; \mathbf{F}_1, \mathbf{F}_2, \dots, \mathbf{F}_d]$.

```

1 Set  $\mathcal{C} \leftarrow \mathcal{X}$ ;
2 for  $v = 1, 2, \dots, \text{length}(\rho)$  do
3   Set  $\mathbf{A} \leftarrow \mathcal{C}_{(\rho_v)}$ ,  $n = \text{size}(\mathbf{A}, 2)$ ;
4   Draw a Gaussian random matrix  $\mathbf{G} \in \mathbb{R}^{n \times b_{\rho_v}}$ ;
5   Build the Krylov subspace:
6    $\mathbf{K} := [\mathbf{A}\mathbf{G}, (\mathbf{A}\mathbf{A}^T)\mathbf{A}\mathbf{G}, \dots, (\mathbf{A}\mathbf{A}^T)^{q_{\rho_v}}\mathbf{A}\mathbf{G}]$ ;
7   Form an orthonormal basis  $\mathbf{Z}$  for  $\mathbf{K}$ ;
8   Compute  $\mathbf{M} := \mathbf{Z}^T \mathbf{A} \mathbf{A}^T \mathbf{Z}$ ;
9   Set  $\mathbf{U}_r$  to the  $r$  top singular vectors of  $\mathbf{M}$ ;
10  Update  $\mathbf{F}_{\rho_v} \leftarrow \mathbf{Z} \mathbf{U}_r$ ,  $\mathbf{C}_{(\rho_v)} \leftarrow (\mathbf{F}_{\rho_v})^T \mathbf{C}_{(\rho_v)}$ ;
11   $\mathcal{C}^{(v)} \leftarrow \mathcal{C}_{(\rho_v)}$ , in tensor format.
12 end
```

Algorithm 2: Deflated QR, $\text{defl-QR}(\mathbf{A}, \delta)$.

Input: $\mathbf{A} \in \mathbb{R}^{m \times n}$, deflation tolerance: δ .

```

1 Compute the pivoted QR factorization:  $\mathbf{A}\mathbf{P} = \tilde{\mathbf{Q}}\tilde{\mathbf{R}}$ ;
2 Find the largest  $s$  such that  $|\tilde{\mathbf{R}}(s, s)| \geq \delta$ ;
3  $\mathbf{R} = \tilde{\mathbf{R}}(1 : s, :) \mathbf{P}^T$ ;
4  $\mathbf{Q} = \tilde{\mathbf{Q}}(:, 1 : s)$ ;
Output:  $\mathbf{Q}, \mathbf{R}, s$ .
```

R-THOSVD and R-STHOSVD) via the *randomized SVD* (R-SVD). Nevertheless, when the singular spectrum of unfolding matrices of original tensor decays slowly, basic R-SVD may produce a poor basis in many applications. Although the R-SVD algorithm using the power iteration strategy can improve the singular value decay rate [75]–[79], it only uses the result of the last iteration rather than the results of each iteration. So it can not always approach the largest k singular values well in general. Motivated by the recently achieved research findings [86]–[88], this subsection first considers integrating the *randomized block Krylov iteration* (RBKI) method into STHOSVD algorithm to accelerate the computation speed. Please see Algorithm 1 for more details. Note that although STHOSVD has the same worst case error-bound as THOSVD, it is less computationally complex and requires less storage [84], [85]. Therefore, in this paper, only the randomized versions of the STHOSVD algorithm is taken into account.

For the proposed fast STHOSVD algorithm using RBKI approach, we had to assume prior knowledge of the target rank (r_1, r_2, \dots, r_d) . Nevertheless, in practical applications, an estimation of the target rank may not be a tractable task. In response to the above issues, in virtue of randomized projection technique and block Lanczos bidiagonalization process method, this subsection sequentially considers investigating an adaptive R-STHOSVD algorithm with prescribed accuracy (i.e., the fixed-accuracy LRTA in the Tucker format). Wherein, the desired truncation rank (r_1, r_2, \dots, r_d) is not known in advance, but we instead want to find a good approximation $\hat{\mathcal{X}}$ such that $\|\mathcal{X} - \hat{\mathcal{X}}\|_F \leq \epsilon$ for some tolerance ϵ . Extensions of

Algorithm 3: Adaptive Randomized STHOSVD Using Block Lanczos Bidiagonalization Process Method, **AD-RSTHOSVD-BLBP**.

Input: $\mathcal{X} \in \mathbb{R}^{n_1 \times \dots \times n_d}$, relative error: ϵ , block size: b , deflation tolerance: δ , processing order: ρ .

Output: $\hat{\mathcal{X}} = [\mathcal{C}; \mathbf{F}_1, \mathbf{F}_2, \dots, \mathbf{F}_d]$.

```

1 Set  $\mathcal{C} \leftarrow \mathcal{X}$ ;
2 for  $v = 1, 2, \dots, \text{length}(\rho)$  do
3   Set  $\mathbf{A} \leftarrow \mathcal{C}_{(\rho_v)}$ ,  $n = \text{size}(\mathbf{A}, 2)$ ;
4   Generate a Gaussian random matrix  $\mathbf{G} \in \mathbb{R}^{n \times b}$ ;
5    $\mathbf{U}^{\{v\}} = [\ ]$ ;  $\mathbf{B}^{\{v\}} = [\ ]$ ;  $\mathbf{V}^{\{v\}} = [\ ]$ ;
6    $E = \|\mathbf{A}\|_F^2$ ;
7    $\mathbf{V}^{(1)} = \text{qr}(\mathbf{G}, 0)$ ;
8    $\mathbf{U}^{(1)} = \mathbf{0}$ ;  $\mathbf{L}^{(1)} = \mathbf{0}$ ;
9    $\mathbf{V}^{\{v\}} = \mathbf{V}^{(1)}$ ;  $\mathbf{U}^{\{v\}} = \mathbf{U}^{(1)}$ ;
10  for  $i = 1, 2, 3, \dots$  do
11     $[\mathbf{U}^{(i)}, \mathbf{R}^{(i)}] =$ 
12       $\text{defl-QR}(\mathbf{A}\mathbf{V}^{(i)} - \mathbf{U}^{(i-1)}\mathbf{L}^{(i)}, \delta)$ ;
13     $\mathbf{U}^{\{v\}} = [\mathbf{U}^{\{v\}}; \mathbf{U}^{(i)}]$ ;
14     $E = E - \|\mathbf{R}^{(i)}\|_F^2$ ;
15     $\mathbf{V}^{(i+1)} = \mathbf{A}^T \mathbf{U}^{(i)} - \mathbf{V}^{(i)} \mathbf{R}^{(i)T}$ ;
16     $\mathbf{V}^{(i+1)} = \mathbf{V}^{(i+1)} - \mathbf{V}^{\{v\}} \mathbf{V}^{\{v\}T} \mathbf{V}^{(i+1)}$ ;
17     $[\mathbf{V}^{(i+1)}, (\mathbf{L}^{(i+1)})^T, s] = \text{defl-QR}(\mathbf{V}^{(i+1)}, \delta)$ ;
18     $\mathbf{V}^{\{v\}} = [\mathbf{V}^{\{v\}}; \mathbf{V}^{(i+1)}]$ ;
19    if  $s < b$  then
20      Draw a random standard Gaussian matrix
21       $\mathbf{G}^{(i)} \in \mathbb{R}^{n \times (b-s)}$ ;
22       $\mathbf{V}'^{(i+1)} = \text{qr}(\mathbf{G}^{(i)} - \mathbf{V}^{\{v\}} \mathbf{V}^{\{v\}T} \mathbf{G}^{(i)})$ ;
23       $\mathbf{V}^{\{v\}} = [\mathbf{V}^{\{v\}}; \mathbf{V}'^{(i+1)}]$ ;
24    end
25     $E = E - \|\mathbf{L}^{(i+1)}\|_F^2$ ;
26    if  $E < \epsilon^2 \|\mathbf{A}\|_F^2$  then
27      break;
28    end
29  end
30  Update  $\mathbf{F}_{\rho_v} \leftarrow \mathbf{U}^{\{v\}}$ ,  $\mathbf{C}_{(\rho_v)} \leftarrow (\mathbf{F}_{\rho_v})^T \mathbf{C}_{(\rho_v)}$ ;
31   $\mathcal{C}^{(v)} \leftarrow \mathcal{C}_{(\rho_v)}$ , in tensor format.
32 end
```

Algorithm 1 to the fixed-accuracy LRTA problem make use of the fact that the Tucker factor matrices can be computed incrementally rather than all at once. The process can then be terminated once a user-specified error threshold has been reached, assuming the error can be efficiently computed or estimated. Please see Algorithm 3 for details.

B. Theoretical Error Bound Analysis

In this subsection, we provide the theoretical error bounds of fixed-rank LRTA algorithm using small-block Krylov iteration method (see Algorithm 1) and fixed-accuracy LRTA algorithm using block Lanczos bidiagonalization process (see Algorithm 3) under the Frobenius norm, respectively. The detailed proofs of our main theories (i.e., Theorems III.1–III.2) can be found in the Supplementary Material.

Definition III.1. Fix block size $b \in [k]$. For each $i \in [k]$, we let $\mathcal{N}_i \subset [k] \setminus \{i\}$ be the indices of the $b - 1$ singular values other than i that minimize $|\frac{\sigma_i(\mathbf{A}) - \sigma_j(\mathbf{A})}{\sigma_j(\mathbf{A})}|$. Then let $g_{\min, b}$ be

the b^{th} -order gap of \mathbf{A} :

$$g_{\min,b}(\mathbf{A}) = \min_{i \in [k]} \min_{j \in [k] \setminus \{i\}} \left| \frac{\sigma_i(\mathbf{A}) - \sigma_j(\mathbf{A})}{\sigma_j(\mathbf{A})} \right|.$$

Theorem III.1. For any order- d tensor $\mathbf{X} \in \mathbb{R}^{n_1 \times n_2 \times \dots \times n_d}$ and $\mathbf{b}_i \leq \mathbf{r}_i$, $i = 1, 2, \dots, d$, let $g_{\min, \mathbf{b}_i}(\mathbf{X}_{(i)})$ as in Definition III.1. For any $\varepsilon, \delta \in (0, 1)$, $q_i = \mathcal{O}\left(\frac{r_i - b_i}{\sqrt{\varepsilon}} \log\left(\frac{1}{g_{\min, \mathbf{b}_i}(\mathbf{X}_{(i)})}\right) + \frac{1}{\sqrt{\varepsilon}} \log\left(\frac{n_i}{\delta \varepsilon}\right)\right)$, Algorithm 1 with processing order $\rho := \{1, 2, \dots, d\}$ returns the low multilinear rank- (r_1, r_2, \dots, r_d) approximation of \mathbf{X} : $\hat{\mathbf{X}} = \mathbf{C}_{\times 1} \mathbf{F}_1 \times_2 \mathbf{F}_2 \dots \times_d \mathbf{F}_d$ such that, with probability at least $1 - \delta$,

$$\|\mathbf{X} - \hat{\mathbf{X}}\|_F / \sqrt{d} \leq (1 + \varepsilon) \|\mathbf{X} - \hat{\mathbf{X}}_{\text{opt}}\|_F, \quad (6)$$

where $\hat{\mathbf{X}}_{\text{opt}}$ denotes the optimal rank- \mathbf{r} approximation.

Definition III.2. Suppose that the number of internal iterations of Algorithm 3 is K . Then, the local loss of orthogonality of factor matrix $\mathbf{F}_v := \mathbf{U}^{\{v\}} = [\mathbf{U}^{(1)}, \dots, \mathbf{U}^{(K)}]$, $v = 1, 2, \dots, d$ is defined as

$$\varepsilon_v = \max \left\{ \max_{1 \leq i \leq K} \|(\mathbf{U}^{(i)})^T \cdot \mathbf{U}^{(i)} - \mathbf{I}\|_2, \max_{2 \leq i \leq K} \|(\mathbf{U}^{(i-1)})^T \cdot \mathbf{U}^{(i)}\|_2 \right\}.$$

The main idea is that we do not require $\|(\mathbf{U}^{(i)})^T \cdot \mathbf{U}^{(i)} - \mathbf{I}\|_2$ to be small. Instead, we need only the milder condition that adjacent blocks be close to orthogonal.

Theorem III.2. Let $\hat{\mathbf{X}} = \mathbf{C}_{\times 1} \mathbf{F}_1 \times_2 \mathbf{F}_2 \dots \times_d \mathbf{F}_d$, $\mathbf{U}^{\{j\}}$, $\mathbf{B}^{\{j\}}$, and $\mathbf{V}^{\{j\}}$ be as produced by Algorithm 3 with input $\mathbf{X} \in \mathbb{R}^{n_1 \times \dots \times n_d}$, deflation tolerance δ and processing order $\rho = [1, 2, \dots, d]$. Let $E_j = \|\mathbf{C}_{(j)}^{(j-1)}\|_F^2 - \|\mathbf{B}^{\{j\}}\|_F^2$, ε_j denote the local loss of orthogonality of $\mathbf{U}^{\{j\}}$, and ϖ_j be the number of columns removed from $\mathbf{U}^{\{j\}}$ due to deflation operation. Assume that $\mathbf{V}^{\{j\}}$ has orthonormal columns. Then

$$\begin{aligned} \|\mathbf{X} - \hat{\mathbf{X}}\|_F^2 &\leq \sum_{j=1}^d \left\{ E_j + (1 + 4\varepsilon_j - \varepsilon_j^2) \|\mathbf{X}_{(j)}\|_F^2 \right. \\ &\quad \left. + 2\delta\sqrt{\varpi_j}(1 + 3\varepsilon_j + 2\varepsilon_j^2) \|\mathbf{X}_{(j)}\|_F \right\}. \end{aligned} \quad (7)$$

Remark III.1. The above theoretical results say that the error bounds for Algorithm 1 and Algorithm 3 are all independent of the processing order. This means that while some processing orders may lead to more accurate decompositions, every processing order has the same worst case error bound. Theorem III.2 shows that as long as the local orthogonality is maintained for factor matrix $\{\mathbf{F}_j\}_{j=1}^d$ and as long as the number of deflations is not too large, we can expect $\sum_{j=1}^d E_j$ to remain an accurate estimate of the Frobenius norm approximation error; at least when the error tolerance is not too small. Thus, we conclude that even if we use one-side reorthogonalization (i.e., only reorthogonalize $\{\mathbf{V}^{\{j\}}\}_{j=1}^d$ regardless of the orthogonality of $\{\mathbf{U}^{\{j\}}\}_{j=1}^d$), the quantity $\sum_{j=1}^d E_j$ will remain a reliable estimate of the approximation error. Note that the above randomized LRTA algorithms and corresponding theoretical analysis can degenerate to existing results presented in matrix format [66], [87], [88].

IV. GENERALIZED NONCONVEX TENSOR MODELING

A. Generalized Nonconvex Regularizers

1) Novel regularizer encoded both L+S priors: In many application scenarios, the large-scale high-order tensors to be estimated are not only with low-rankness but also possess significant smooth structure. Existing purely low-rank based methods are not sufficient to adequately meet the accuracy requirement when facing these simultaneous low-rank and smooth data [16], [29]–[31], [51]–[53]. Besides, previous works on simultaneous L+S tensor recovery typically encoded the L+S prior features coexisting in tensor data as two separate regularization terms (i.e., low-rank term plus total variation term), and then coupled them into various tensor recovery models through additive combination [32], [89], [90]. However, the trade-off parameter between these two terms is tricky to be selected for achieving or approaching the Pareto optimality. Recently, Wang et al. [14] proposed a novel regularization term termed Tensor Correlated Total Variation (T-CTV), which inherently characterizes both L and S priors of a tensor simultaneously. Nevertheless, the T-CTV regularizer was established by the HTNN [29] in the gradient domain, which equally treats all singular components of each gradient tensor in the transform domain, thus causing some unavoidable biases in practical application. To address simultaneous L+S large-scale tensor recovery problem more effectively and flexibly, we propose a unified nonconvex regularization strategy that is tighter for T-SVD rank approximation.

Below, based on the shortcomings of existing prior characterization paradigms [14], [32], [89], [90], we define the following *Generalized Nonconvex High-Order T-CTV* (GN-HTCTV) regularizer:

Definition IV.1. (Gradient tensor [14]) For $\mathcal{A} \in \mathbb{R}^{n_1 \times \dots \times n_d}$, its gradient tensor along the k -th mode is defined as

$$\mathcal{G}_k := \nabla_k(\mathcal{A}) = \mathcal{A} \times_k \mathbf{D}_{n_k}, \quad k = 1, 2, \dots, d, \quad (8)$$

where \mathbf{D}_{n_k} is a row circulant matrix of $(-1, 1, 0, \dots, 0)$, and ∇_k is defined as the corresponding difference operator along the k -th mode of tensor \mathcal{A} .

Definition IV.2. (GNHTCTV) Let \mathfrak{L} be any invertible linear transform in (1) and its corresponding transform matrices satisfy (2). For $\mathcal{A} \in \mathbb{R}^{n_1 \times \dots \times n_d}$, denote Γ as a priori set consisting of directions along which \mathcal{A} equips L+S priors, and \mathcal{G}_k , $k \in \Gamma$ as its correlated gradient tensors. Then, the GNHTCTV norm is defined as

$$\Psi(\mathcal{A}) := \frac{1}{\gamma} \sum_{k \in \Gamma} \|\nabla_k(\mathcal{A})\|_{\Phi, \mathfrak{L}} = \frac{1}{\gamma} \sum_{k \in \Gamma} \left(\frac{1}{\rho} \sum_{i=1}^m \sum_{j=1}^n \Phi(\sigma_{ij}^{(k)}) \right),$$

where $\gamma := \#\{\Gamma\}$ equals to the cardinality of Γ , $m = \min(n_1, n_2)$, $n = n_3 \dots n_d$, $\rho = \alpha_3 \dots \alpha_d > 0$ represents a constant determined by \mathfrak{L} , \mathcal{S}_k is the middle component of $\nabla_k(\mathcal{A}) = \mathbf{U}_k *_{\mathfrak{L}} \mathcal{S}_k *_{\mathfrak{L}} \mathbf{V}_k^T$, $\sigma_{ij}^{(k)} = \mathfrak{L}(\mathcal{S}_k)^{<j>}(i, i)$, and $\Phi(\cdot) : \mathbb{R}^+ \rightarrow \mathbb{R}^+$ is a generalized nonconvex function.

Assumption IV.1. The generalized nonconvex function $\Phi(\cdot) : \mathbb{R}^+ \rightarrow \mathbb{R}^+$ satisfies the following assumptions:

- **(I):** $\Phi(\cdot): \mathbb{R}^+ \rightarrow \mathbb{R}^+$ is proper, lower semi-continuous and symmetric with respect to y-axis;
- **(II):** $\Phi(\cdot)$ is concave and monotonically increasing on $[0, \infty)$ with $\Phi(0) = 0$.

If there is no special explanation, we suppose that Assumption IV.1 holds throughout the paper.

Many popular nonconvex penalty functions satisfy the above Assumption IV.1, such as firm function [91], logarithmic (Log) function [92], ℓ_q function [93], smoothly clipped absolute deviation (SCAD) function [94], and minimax concave penalty (MCP) function [95], capped- ℓ_q function [96], [97]. Thus, the novel proposed GNHTCTV regularizer is equivalent to employing a family of nonconvex functions onto the singular values of all face slices of each gradient tensor in the transformed domain. Many existing regularizers (e.g., [14], [16], [29], [38], [41], [42], [54]–[59], [98]–[100]) can be regarded as specialized instances of our GNHTCTV. For example, when $\Phi(\cdot)$ is set to the ℓ_1 -norm, the GNHTCTV regularizer degenerates to the T-CTV norm proposed in [14], i.e.,

$$\|\mathcal{A}\|_{T-CTV} := \frac{1}{\gamma} \sum_{k \in \Gamma} \|\mathcal{G}_k\|_{\otimes, \mathcal{L}},$$

where $\|\cdot\|_{\otimes, \mathcal{L}}$ denotes the *high-order TNN* (HTNN) [29], i.e., $\|\mathcal{A}\|_{\otimes, \mathcal{L}} := \frac{1}{\rho} \|\text{bdiag}(\mathcal{A}_{\mathcal{L}})\|_*$, where $\rho = \alpha_3 \cdots \alpha_d$.

2) **Novel noise/outliers regularizer:** Related studies indicate that the ℓ_1 -norm sometimes is biased and statistically suboptimal in enhancing the robustness against noise/outliers. Besides, real-world tensor data may also be corrupted by other structured noise/outliers (e.g., slice-wise and tube-wise format) other than the entry-wise form. Owing to the aforementioned facts, we hence define the following generalized nonconvex noise/outliers regularization penalty:

$$\Upsilon(\mathcal{E}) := \psi(h(\mathcal{E})), \quad (9)$$

where $\psi(\cdot): \mathbb{R}^+ \rightarrow \mathbb{R}^+$ is a generalized nonconvex function, which has the same properties as $\Phi(\cdot)$. Here, three type of corrupted noise/outliers are taken into account: **1)** When the tensor \mathcal{E} is an entry-wise noise/outlier tensor, and then $h(\cdot) = \|\cdot\|_{\ell_1}$ is defined as an ℓ_1 -norm; **2)** When the noise/outlier tensor \mathcal{E} has tube-wise structure, and then $h(\cdot) = \|\cdot\|_{\text{tube}_1}$ is defined as an tube_1 -norm; **3)** When the tensor \mathcal{E} has structured noise/outlier on the slices, and then $h(\cdot) = \|\cdot\|_{\text{slice}_1}$ is defined as an slice_1 -norm.

B. Fast Generalized Solver for Key Subproblems

This subsection presents the solution method of two kinds of key subproblems involved in subsequent models, i.e.,

$$\arg \min_{\mathcal{E}} \lambda \cdot \Upsilon(\mathcal{E}) + \frac{1}{2} \|\mathcal{E} - \mathcal{A}\|_F^2, \quad (10)$$

$$\arg \min_{\mathcal{G}} \tau \cdot \|\mathcal{G}\|_{\Phi, \mathcal{L}} + \frac{1}{2} \|\mathcal{G} - \mathcal{A}\|_F^2. \quad (11)$$

1) **Solve the problem (10) via GNHTT Operator:** Before providing the solution to the problem (10), we first introduce the proximal mappings of the generalized nonconvex functions, which plays a central role in developing highly efficient first-order algorithms. Specifically, for a nonconvex

penalty function $\psi(\cdot)$ satisfying Assumption IV.1, its proximity operator is defined as

$$\text{Prox}_{\psi, \mu}(v) = \arg \min_x \left\{ \mu \cdot \psi(x) + \frac{1}{2} (x - v)^2 \right\}, \quad (12)$$

where $\mu > 0$ is a penalty parameter.

In the supplementary material, we summarize the proximity operator for several popular nonconvex regularization penalties satisfying Assumption IV.1, including firm-thresholding, ℓ_q -thresholding, capped- ℓ_q thresholding, MCP, Log, and SCAD penalties. Based on the previous analysis, the optimal solution to the subproblem (10) can be computed by *generalized nonconvex high-order tensor thresholding/shrinkage* (GNHTT) operator in an element-wise, tube-wise or slice-wise manner. Specifically, if $h(\cdot) = \|\cdot\|_{\ell_1}$, then we have

$$\hat{\mathcal{E}}_{i_1 \dots i_d} = \text{Prox}_{\psi, \lambda}(\mathcal{A}_{i_1 \dots i_d}), \forall (i_1, \dots, i_d) \in [n_1] \times \dots \times [n_d].$$

If $h(\cdot) = \|\cdot\|_{\text{tube}_1}$, then we have

$$\hat{\mathcal{E}}_{ij, \dots} = \frac{\mathcal{A}_{ij, \dots}}{\|\mathcal{A}_{ij, \dots}\|_F} \cdot \text{Prox}_{\psi, \lambda}(\|\mathcal{A}_{ij, \dots}\|_F), \forall (i, j) \in [n_1] \times [n_2].$$

If $h(\cdot) = \|\cdot\|_{\text{slice}_1}$, then we have

$$\hat{\mathcal{E}}^{<k>} = \frac{\mathcal{A}^{<k>}}{\|\mathcal{A}^{<k>}\|_F} \cdot \text{Prox}_{\psi, \lambda}(\|\mathcal{A}^{<k>}\|_F), \forall k \in [n_3 \cdots n_d].$$

2) Solve the problem (11) via GNHTSVT Operator:

Before providing the solution to the problem (11), we first introduce the following key definition and theorem.

Definition IV.3. (GNHTSVT operator) Let $\mathcal{A} = \mathcal{U}_{* \mathcal{L}} \mathcal{S}_{* \mathcal{L}} \mathcal{V}^T$ be the T-SVD of $\mathcal{A} \in \mathbb{R}^{n_1 \times \dots \times n_d}$, $m = \min(n_1, n_2)$, and $n = n_3 \cdots n_d$. For any $\tau > 0$, then the Generalized Nonconvex High-Order Tensor Singular Value Thresholding (GNHTSVT) operator of \mathcal{A} is defined as follows

$$\mathcal{D}_{\Phi, \tau}(\mathcal{A}, \mathcal{L}) = \mathcal{U}_{* \mathcal{L}} \mathcal{S}_{\Phi, \tau} \mathcal{V}^T, \quad (13)$$

where $\mathcal{S}_{\Phi, \tau}^{<j>}(i, i) = \text{Prox}_{\Phi, \tau}(\mathcal{S}^{<j>}(i, i))$ for $j = 1, 2, \dots, n$, $i = 1, 2, \dots, m$, and $\text{Prox}_{\Phi, \tau}(\cdot)$ denotes the proximity operator of nonconvex penalty function $\Phi(\cdot)$, which has the same properties as $\psi(\cdot)$.

Theorem IV.1. Let \mathcal{L} be any invertible linear transform in (1) and its transform matrices satisfy (2), $m = \min(n_1, n_2)$, $n = n_3 n_4 \cdots n_d$. For any $\tau > 0$ and $\mathcal{A} \in \mathbb{R}^{n_1 \times \dots \times n_d}$, if the nonconvex penalty function $\Phi(\cdot)$ satisfies Assumption IV.1, then GNHTSVT operator (13) obeys

$$\mathcal{D}_{\Phi, \tau}(\mathcal{A}, \mathcal{L}) = \arg \min_{\mathcal{G}} \tau \cdot \|\mathcal{G}\|_{\Phi, \mathcal{L}} + \frac{1}{2} \|\mathcal{G} - \mathcal{A}\|_F^2. \quad (14)$$

According to the above Definition IV.3 and Theorem IV.1, the subproblem (11) can be efficiently solved in virtue of GNHTSVT operation.

3) **Fast Randomized GNHTSVT:** We can find that when dealing with large-scale high-order tensor data, the major bottleneck of solving the minimization problem (11) is to compute the GNHTSVT operator involving time-consuming T-SVD multiple times. To address this issue, by the R-STHOSVD-BKI and AD-RSTHOSVD-BLBP algorithms leveraging full-mode random projection, Krylov subspace iteration and block

Algorithm 4: Accelerated GNHTSVT operation.

Input: $\mathcal{A} \in \mathbb{R}^{n_1 \times \dots \times n_d}$, processing order: ρ , transform: \mathcal{L} , regularizer: $\Phi(\cdot)$, $\tau > 0$, target rank: r , block size in Algorithm 1: b , Krylov iterations: q , block size in Algorithm 3: b , error tolerance: ϵ , deflation tolerance: δ .

```

1 if not utilize the randomized technique then
2   Compute the results of  $\mathcal{L}$  on  $\mathcal{A}$ , i.e.,  $\mathcal{L}(\mathcal{A})$ ;
3   for  $v = 1, 2, \dots, n_3 n_4 \dots n_d$  do
4      $[\mathcal{L}(\mathcal{U})^{<v>}, \mathcal{L}(\mathcal{S})^{<v>}, \mathcal{L}(\mathcal{V})^{<v>}] =$ 
        $\text{svd}(\mathcal{L}(\mathcal{A})^{<v>})$ ;
5      $\tilde{\mathcal{S}} = \text{Prox}_{\Phi, \tau} [\text{diag}(\mathcal{L}(\mathcal{S})^{<v>})]$ ;
6      $\mathcal{L}(\mathcal{C})^{<v>} = \mathcal{L}(\mathcal{U})^{<v>} \cdot \text{diag}(\tilde{\mathcal{S}}) \cdot (\mathcal{L}(\mathcal{V})^{<v>})^T$ ;
7   end
8    $\mathcal{D}_{\Phi, \tau}(\mathcal{A}, \mathcal{L}) \leftarrow \mathcal{L}^{-1}(\mathcal{L}(\mathcal{C}))$ .
9 end
10 else if utilize the randomized technique then
11   Obtain  $\mathcal{A} = [\mathcal{C}; \mathcal{F}_1, \mathcal{F}_2, \dots, \mathcal{F}_d]$  by Algorithm 1 or
     Algorithm 3;
12   Perform the deterministic GNHTSVT operation on
     Tucker core tensor  $\mathcal{C}$ , i.e.,  $\tilde{\mathcal{C}} = \mathcal{D}_{\Phi, \tau}(\mathcal{C}, \mathcal{L})$ ;
13    $\mathcal{D}_{\Phi, \tau}(\mathcal{A}, \mathcal{L}) = \tilde{\mathcal{C}} \times_1 \mathcal{F}_1 \times_2 \mathcal{F}_2 \dots \times_d \mathcal{F}_d$ .
14 end

```

Lanczos bidiagonalization strategies, a fast and efficient randomized method is suggested to boost the computational speed of GNHTSVT operator (please see Algorithm 4 for details). Specifically, the adaptive randomized Tucker compression algorithm is first applied to the original large-scale high-order tensor. Then, the deterministic GNHTSVT operation is employed to the small-scale core tensor generated by randomized Tucker decomposition. Finally, obtain the approximation tensor by back projection of the factor matrices in Step 1 and the result of GNHTSVT operation in Step 2. Please see Line 11-13 in Algorithm 4 for details. The main idea is utilizing the randomized Tucker factorization in the first step as a preprocessing step after which the deterministic algorithms can be applied to the smaller Tucker core tensor.

V. TYPICAL APPLICATIONS

A. Unquantized Tensor Recovery

In this subsection, we consider two typical nonquantized tensor recovery tasks: 1) Noisy tensor completion; 2) Noise-free tensor completion.

1) **Generalized Nonconvex Model:** Based on the designed generalized nonconvex regularizers (see Subsection IV-A), a novel model named Generalized Nonconvex Robust High-Order Tensor Completion (GNRHTC) is proposed in this paper. Mathematically, the proposed GNRHTC model can be formulated as follows:

$$\min_{\mathcal{L}, \mathcal{E}} \Psi(\mathcal{L}) + \lambda \Upsilon(\mathcal{E}), P_{\Omega}(\mathcal{L} + \mathcal{E}) = P_{\Omega}(\mathcal{M}), \quad (15)$$

where $P_{\Omega}(\cdot)$ is the projection operator onto the observed index set Ω , $\Psi(\mathcal{L})$ represents the regularizer measuring tensor low-rankness plus smoothness properties concurrently, $\Upsilon(\mathcal{E})$ denotes the noise/outliers regularization (see Subsection IV-A for details), and $\lambda > 0$ is a trade-off parameter that balances these two regularization terms. Broadly speaking, the advantages of GNRHTC model are summarized as follows:

1) The optimization problems formulated in existing works (e.g., [14], [16], [29], [38], [40], [41], [50], [54]–[56], [58], [59], [98]–[102]) can be viewed as special cases of our GNRHTC. For example, 1) Our proposed model (15) is equivalent to the NRTRM model [55] or GNCM-RTC model [100], when the tensor's order is set to 3 and the local smoothness is not taken into account; 2) Furthermore, on the basis of the above conditions, if an additional condition is attached, i.e., Ω is the whole observed set, then our proposed model (15) can reduce to the GNR model [102]; 3) When the generalized regularization terms are respectively set to be the T-CTV norm and ℓ_1 -norm, i.e., $\Psi(\mathcal{L}) = \|\mathcal{L}\|_{T-CTV}$, $\Upsilon(\mathcal{E}) = \|\mathcal{E}\|_1$, and Ω is the whole indices set, then our formulated model (15) degenerates to the T-CTV-TRPCA model [14].

2) Compared with the existing RLRTC approaches (e.g., [16], [54]–[56], [58], [59], [99], [100]) within the T-SVD framework, the GNRHTC method consider a more unified, realistic and challenging situation. Specifically, the GNRHTC model can well process the tensor data with arbitrary order degraded by elements loss and noise/outliers corruption. Besides, two novel generalized nonconvex regularizers $\Psi(\cdot)$ and $\Upsilon(\cdot)$ are integrated into the GNRHTC model, the former can synchronously encode both \mathbf{L} and \mathbf{S} priors of a tensor into a unique concise form, and the latter is capable of processing several types of popular structured noise/outliers tensors, like entries-wise, slice-wise and tube-wise forms. Existing approaches rarely achieve these goals simultaneously.

Remark V.1. When we disregard the noise scenario (i.e., the trade-off parameter λ is set to zero), the proposed model (15) degenerates into the following generalized nonconvex high-order tensor completion (GNHTC) model:

$$\begin{aligned} \min_{\mathcal{L}, \mathcal{G}_k} \frac{1}{\gamma} \sum_{k \in \Gamma} \|\mathcal{G}_k\|_{\Phi, \mathcal{L}}, \\ \text{s.t. } \mathcal{G}_k = \nabla_k(\mathcal{L}), \quad P_{\Omega}(\mathcal{L}) = P_{\Omega}(\mathcal{M}). \end{aligned} \quad (16)$$

Existing robust matrix completion (RMC) methods (e.g., [103]–[108]) are limited to the case of matrix data. These efforts requires to reshape the raw data into a large-scale matrix when dealing with high-order tensor data. Wherein, the matricization operator destroys the intrinsic structure of the original tensor data, thus resulting in unsatisfied recovery performance. On the contrary, the proposed GNHTC and GNRHTC models (15)–(16) are able to work directly with raw tensor data without any expansion. Thus, it preserves the intrinsic structure of the original tensor data very well, and adequately characterizes its spatial-spectral correlation.

2) **Optimization Algorithm:** In this subsection, the ADMM framework [109] is adopted to solve the proposed models (15) and (16). Given the significant similarities in the ADMM optimization procedures between the two models, we will only provide the detailed steps for the former. The nonconvex model (15) can be equivalently reformulated as follows:

$$\begin{aligned} \min_{\mathcal{L}, \mathcal{E}, \mathcal{G}_k} \frac{1}{\gamma} \sum_{k \in \Gamma} \|\mathcal{G}_k\|_{\Phi, \mathcal{L}} + \lambda \Upsilon(P_{\Omega}(\mathcal{E})), \\ \text{s.t. } \mathcal{G}_k = \nabla_k(\mathcal{L}), \quad \mathcal{L} + \mathcal{E} = \mathcal{M}, \end{aligned} \quad (17)$$

The augmented Lagrangian function of (17) is

$$\begin{aligned} \mathcal{F}(\mathcal{L}, \{\mathcal{G}_k, k \in \Gamma\}, \mathcal{E}, \{\Lambda_k, k \in \Gamma\}, \mathbf{y}) = & \sum_{k \in \Gamma} \left(\frac{1}{\gamma} \|\mathcal{G}_k\|_{\Phi, \mathcal{L}} + \right. \\ & \left. \langle \Lambda_k, \nabla_k(\mathcal{L}) - \mathcal{G}_k \rangle + \frac{\mu}{2} \|\nabla_k(\mathcal{L}) - \mathcal{G}_k\|_F^2 \right) + \lambda \Upsilon(P_\Omega(\mathcal{E})) + \\ & \langle \mathbf{y}, \mathcal{M} - \mathcal{L} - \mathcal{E} \rangle + \frac{\mu}{2} \|\mathcal{M} - \mathcal{L} - \mathcal{E}\|_F^2, \end{aligned} \quad (18)$$

where μ is the regularization parameter, and $\{\Lambda_k, k \in \Gamma\}$, \mathbf{y} are Lagrange multipliers. It can be further expressed as

$$\begin{aligned} \mathcal{F}(\mathcal{L}, \{\mathcal{G}_k, k \in \Gamma\}, \mathcal{E}, \{\Lambda_k, k \in \Gamma\}, \mathbf{y}) = & \lambda \Upsilon(P_\Omega(\mathcal{E})) + \\ & \sum_{k \in \Gamma} \left(\frac{1}{\gamma} \|\mathcal{G}_k\|_{\Phi, \mathcal{L}} + \mu/2 \|\nabla_k(\mathcal{L}) - \mathcal{G}_k + \Lambda_k/\mu\|_F^2 \right) + \\ & \frac{\mu}{2} \|\mathcal{M} - \mathcal{L} - \mathcal{E} + \mathbf{y}/\mu\|_F^2 + C, \end{aligned} \quad (19)$$

where C is only the multipliers dependent squared items. Below, we show how to solve the subproblems for each involved variable.

Update $\mathcal{L}^{\{t+1\}}$ (low-rank component) Taking the derivative in (19) with respect to \mathcal{L} , it gets the following linear system:

$$\begin{aligned} \left(\mathcal{J} + \sum_{k \in \Gamma} \nabla_k^T \nabla_k \right) (\mathcal{L}) = & (\mathcal{M} - \mathcal{E}^{\{t\}} + \frac{\mathbf{y}^{\{t\}}}{\mu^{\{t\}}}) + \sum_{k \in \Gamma} \\ & \nabla_k^T (\mathcal{G}_k^{\{t\}} - \Lambda_k^{\{t\}}/\mu^{\{t\}}), \end{aligned} \quad (20)$$

where $\nabla_k^T(\cdot)$ denotes the transpose operator of $\nabla_k(\cdot)$. Note that the difference operation on tensors has been proved to be linear via high-order t-product [14]. Referring to the literature [110], we can apply multi-dimensional FFT, which diagonalizes $\nabla_k(\cdot)$'s corresponding difference tensors \mathcal{D}_k , enabling to efficiently obtain the optimal solution of (20) in virtue of convolution theorem of Fourier transforms, i.e.,

$$\mathcal{L}^{\{t+1\}} = \mathcal{F}^{-1} \left(\frac{\mathcal{F}(\mathcal{M} - \mathcal{E}^{\{t\}} + \frac{\mathbf{y}^{\{t\}}}{\mu^{\{t\}}}) + \mathcal{J}}{\mathbf{1} + \sum_{k \in \Gamma} \mathcal{F}(\mathcal{D}_k)^H \odot \mathcal{F}(\mathcal{D}_k)} \right), \quad (21)$$

where $\mathcal{J} = \sum_{k \in \Gamma} \mathcal{F}(\mathcal{D}_k)^H \odot \mathcal{F}(\mathcal{G}_k^{\{t\}} - \frac{\Lambda_k^{\{t\}}}{\mu^{\{t\}}})$, $\mathbf{1}$ is a tensor with all elements as 1, \odot is componentwise multiplication, and the division is componentwise as well.

Update $\mathcal{G}_k^{\{t+1\}}$, $k \in \Gamma$ (gradient component) For each $k \in \Gamma$, extracting all items containing \mathcal{G}_k from (18), we can get that

$$\min_{\mathcal{G}_k} \frac{1}{\gamma} \|\mathcal{G}_k\|_{\Phi, \mathcal{L}} + \frac{\mu^{\{t\}}}{2} \|\nabla_k(\mathcal{L}^{\{t+1\}}) - \mathcal{G}_k + \frac{\Lambda_k^{\{t\}}}{\mu^{\{t\}}}\|_F^2. \quad (22)$$

This key subproblem is analogous to the form of the minimization problem (11), and its close-form solution can be efficiently obtained by utilizing the fast randomized GNHTSVT operation. Please see IV-B for details.

Update $\mathcal{E}^{\{t+1\}}$ (noise/outliers component) The optimization subproblem with respect to \mathcal{E} can be written as

$$\min_{\mathcal{E}} \lambda \Upsilon(P_\Omega(\mathcal{E})) + \frac{\mu^{\{t\}}}{2} \|\mathcal{E} - (\mathcal{M} - \mathcal{L}^{\{t+1\}} + \frac{\mathbf{y}^{\{t\}}}{\mu^{\{t\}}})\|_F^2.$$

Let $\mathcal{H}^{\{t\}} = \mathcal{M} - \mathcal{L}^{\{t+1\}} + \frac{\mathbf{y}^{\{t\}}}{\mu^{\{t\}}}$. The above problem can be solved by the following two subproblems with respect to $P_\Omega(\mathcal{E}^{\{t+1\}})$ and $P_{\Omega_\perp}(\mathcal{E}^{\{t+1\}})$, respectively.

Algorithm 5: Solve GNRHTC model (15) via ADMM.

Input: $P_\Omega(\mathcal{M}) \in \mathbb{R}^{n_1 \times \dots \times n_d}$, \mathcal{L} , $\Phi(\cdot)$, $\psi(\cdot)$, $h(\cdot)$, Γ , λ , ρ , \mathbf{b} , \mathbf{q} , ϵ , b , δ .

1 **Initialize:** $\mathcal{G}_k^{\{0\}} = \mathcal{E}^{\{0\}} = \Lambda_k^{\{0\}} = \mathbf{y}^{\{0\}} = \mathbf{0}$, ϑ , $\mu^{\{0\}}$, μ^{\max} , ϖ , $t = 0$;

2 **while not converged do**

3 Update $\mathcal{L}^{\{t+1\}}$ by computing (20) ;

4 Update $\mathcal{G}_k^{\{t+1\}}$ by computing (22) for each $k \in \Gamma$;

5 Update $P_\Omega(\mathcal{E}^{\{t+1\}})$ by computing (23);

6 Update $P_{\Omega_\perp}(\mathcal{E}^{\{t+1\}})$ by computing (24);

7 Update $\Lambda_k^{\{t+1\}}$, $\mathbf{y}^{\{t+1\}}$, $\mu^{\{t+1\}}$ by computing (25)-(27);

8 Check the convergence condition by computing (28).

9 **end**

Output: $\mathcal{L} \in \mathbb{R}^{n_1 \times \dots \times n_d}$.

Regarding $P_\Omega(\mathcal{E}^{\{t+1\}})$: the optimization subproblem with respect to $P_\Omega(\mathcal{E}^{\{t+1\}})$ is formulated as following

$$\min_{P_\Omega(\mathcal{E})} \lambda \Upsilon(P_\Omega(\mathcal{E})) + \frac{\mu^{\{t\}}}{2} \|P_\Omega(\mathcal{E} - \mathcal{H}^{\{t\}})\|_F^2. \quad (23)$$

This subproblem is equivalent to the form of the minimization problem (10), and its close-form solution can be obtained by utilizing the generalized nonconvex shrinkage operator. Please see IV-B for details.

Regarding $P_{\Omega_\perp}(\mathcal{E}^{\{t+1\}})$: the optimization subproblem with respect to $P_{\Omega_\perp}(\mathcal{E}^{\{t+1\}})$ is formulated as following

$$P_{\Omega_\perp}(\mathcal{E}^{\{t+1\}}) = \min_{P_{\Omega_\perp}(\mathcal{E})} \frac{\mu^{\{t\}}}{2} \|P_{\Omega_\perp}(\mathcal{E} - \mathcal{H}^{\{t\}})\|_F^2. \quad (24)$$

The closed-form solution for subproblem (24) can be obtained through the standard least square regression method.

Update $\Lambda_k^{\{t+1\}}$, $k \in \Gamma$, $\mathbf{y}^{\{t+1\}}$, and $\mu^{\{t+1\}}$ (Lagrange multipliers and penalty parameter) Based on the rule of ADMM framework, the lagrange multipliers are updated by the following equations:

$$\mathbf{y}^{\{t+1\}} = \mathbf{y}^{\{t\}} + \mu^{\{t\}} (\mathcal{M} - \mathcal{L}^{\{t+1\}} - \mathcal{E}^{\{t+1\}}), \quad (25)$$

$$\Lambda_k^{\{t+1\}} = \Lambda_k^{\{t\}} + \mu^{\{t\}} (\nabla_k(\mathcal{L}^{\{t+1\}}) - \mathcal{G}_k^{\{t+1\}}), \quad (26)$$

$$\mu^{\{t+1\}} = \min(\mu^{\max}, \vartheta \mu^{\{t\}}), \quad (27)$$

where ϑ stands for the growth rate.

Check the convergence condition: The convergence condition is defined as follows:

$$\max \left\{ \begin{aligned} & \|\mathcal{L}^{\{t+1\}} - \mathcal{L}^{\{t\}}\|_\infty, \|\mathcal{E}^{\{t+1\}} - \mathcal{E}^{\{t\}}\|_\infty \\ & \|\nabla_k \mathcal{L}^{\{t+1\}} - \mathcal{G}_k^{\{t+1\}}\|_\infty, \|\mathcal{G}_k^{\{t+1\}} - \mathcal{G}_k^{\{t\}}\|_\infty \\ & \|\mathcal{M} - \mathcal{L}^{\{t+1\}} - \mathcal{E}^{\{t+1\}}\|_\infty \end{aligned} \right\} \leq \varpi. \quad (28)$$

The whole ADMM optimization scheme is summarized in Algorithm 5. Noting that the time complexity analysis of the proposed algorithms is provided in the supplementary material.

3) **Convergence Analysis:** In this subsection, we provide the convergence analysis of the proposed algorithm. The detailed proofs of relevant theories and lemmas can be found in the Supplementary Material.

Lemma V.1. *The sequences $\{\mathbf{y}^{(t)}\}$ and $\{\Lambda_k^{(t)}, k \in \Gamma\}$ generated by Algorithm 5 are bounded.*

Lemma V.2. *Suppose that the sequences $\{\mathbf{y}^{(t)}\}$ and $\{\Lambda_k^{(t)}, k \in \Gamma\}$ generated by Algorithm 5 are bounded, then the sequence $\{\mathcal{L}^{(t)}, \{\mathcal{G}_k^{(t)}, k \in \Gamma\}, \mathcal{E}^{(t)}\}$ is bounded.*

Theorem V.1. *Suppose that the sequence $\{\mathbf{y}^{(t)}, \Lambda_k^{(t)}, k \in \Gamma\}$ generated by Algorithm 5 is bounded. Then, the sequences $\{\mathcal{L}^{(t+1)}\}$, $\{\mathcal{G}_k^{(t+1)}, k \in \Gamma\}$, and $\{\mathcal{E}^{(t+1)}\}$ satisfy:*

- 1) $\lim_{t \rightarrow \infty} \|\mathcal{M} - \mathcal{L}^{(t+1)} - \mathcal{E}^{(t+1)}\|_F = 0$;
- 2) $\lim_{t \rightarrow \infty} \|\nabla_k(\mathcal{L}^{(t+1)}) - \mathcal{G}_k^{(t+1)}\|_F = 0, k \in \Gamma$;
- 3) $\lim_{t \rightarrow \infty} \|\mathcal{L}^{(t+1)} - \mathcal{L}^{(t)}\|_F = \lim_{t \rightarrow \infty} \|\mathcal{E}^{(t+1)} - \mathcal{E}^{(t)}\|_F = 0$;
- 4) $\lim_{t \rightarrow \infty} \|\mathcal{G}_k^{(t+1)} - \mathcal{G}_k^{(t)}\|_F = 0; k \in \Gamma$.

Theorem V.2. *Let $\{\mathcal{L}^{(t)}, \{\mathcal{G}_k^{(t)}, k \in \Gamma\}, \mathcal{E}^{(t)}, \{\Lambda_k^{(t)}, k \in \Gamma\}, \mathbf{y}^{(t)}\}$ be a sequence generated by Algorithm 5. Suppose that the sequences $\{\mathbf{y}^{(t)}\}$ and $\{\Lambda_k^{(t)}, k \in \Gamma\}$ are bounded. Then, any accumulation point of the sequence $\{\mathcal{L}^{(t)}, \{\mathcal{G}_k^{(t)}, k \in \Gamma\}, \mathcal{E}^{(t)}, \{\Lambda_k^{(t)}, k \in \Gamma\}, \mathbf{y}^{(t)}\}$ is a Karush-Kuhn-Tucker (KKT) point of the optimization problem (17).*

B. Quantized Tensor Recovery

In this subsection, we consider two typical quantized tensor recovery task, i.e., *One-Bit High-Order Tensor Completion* (OBHTC) and *One-Bit Robust High-Order Tensor Completion* (OBRHTC).

1) **Generalized Nonconvex Model:** A novel OBHTC model is investigate from uniformly dithered binary observations. Specifically, let $y_k (\forall k \in [m])$ be the k -th noisy observation from the low-rank tensor $\mathcal{L}^* \in \mathbb{R}^{n_1 \times \dots \times n_d}$ via $y_k = \langle \mathcal{P}_k, \mathcal{L}^* \rangle + \epsilon_k$, where \mathcal{P}_k is the sampler that uniformly and randomly extracts one entry of \mathcal{L}^* , and ϵ_k denotes additive noise independent of \mathcal{P}_k . Then, we propose to quantize y_k to

$$q_k = \text{sign}(y_k + \xi_k),$$

where all dithers $\xi_k, k \in \{1, 2, \dots, m\}$ are uniformly distributed on the interval $[-\theta, \theta]$ with some $\theta > 0$. Based on Proposition II.1, we can utilized θq_k as a substitute for the full observation q_k . Consequently, we propose the following regularized OBHTC model:

$$\hat{\mathcal{L}} = \arg \min_{\|\mathcal{L}\|_\infty \leq \alpha} \frac{1}{2m} \sum_{k=1}^m (\langle \mathcal{P}_k, \mathcal{L} \rangle - \theta q_k)^2 + \lambda \Psi(\mathcal{L}), \quad (29)$$

where λ is the regularization parameter, $\Psi(\cdot)$ is formulated according to Definition IV.2, m denotes the number of observations, and the assumption $\|\mathcal{L}\|_\infty \leq \alpha$ ($\alpha > 0$) helps make the recovery well-posed by preventing excessive “spikiness”.

To handle the incomplete high-order tensor damaged by both Gaussian noise and sparse noise simultaneously, we can extend the Model (29) to the following model:

$$\begin{aligned} \hat{\mathcal{L}} = \arg \min_{\|\mathcal{L}\|_\infty \leq \alpha} & \frac{1}{2m} \sum_{k=1}^m (\langle \mathcal{P}_k, \mathcal{L} + \mathcal{S} \rangle - \theta \hat{q}_k)^2 + \lambda_1 \Psi(\mathcal{L}) \\ & + \lambda_2 \Upsilon(\mathcal{S}), \end{aligned} \quad (30)$$

Algorithm 6: Solve GNOBHTC model (29) via ADMM.

Input: One-bit observations: $\{q_k\}_{\forall k \in [m]}$, uniform samplers: $\mathcal{P}_k (\forall k \in [m])$, $\mathcal{L}, \Phi(\cdot), \Gamma$, $\gamma := \#\{\Gamma\}, \lambda, \theta, \alpha, \rho, \mathbf{b}, \mathbf{q}, \epsilon, b, \delta$.

- 1 **Initialize:** $\mathcal{G}_i^{(0)} = \mathcal{Z}^{(0)} = \Lambda_i^{(0)} = \mathbf{y}^{(0)} = \mathbf{0}$, $\vartheta = 1.05, \mu^{(0)} = 10^{-6}, \mu^{\max} = 10^3, \varpi, t = 0$;
- 2 **while not converged do**
- 3 Update $\mathcal{L}^{(t+1)}$ by computing (32);
- 4 Update $\mathcal{Z}^{(t+1)}$ by computing (33);
- 5 Update $\mathcal{G}_i^{(t+1)}$ by computing (34) for each $i \in \Gamma$;
- 6 Update $\Lambda_i^{(t+1)}, \mathbf{y}^{(t+1)}, \mu^{(t+1)}$ by (35)-(37);
- 7 Check the convergence condition by computing $\|\mathcal{L}^{(t+1)} - \mathcal{L}^{(t)}\|_F / \|\mathcal{L}^{(t)}\|_F \leq \varpi$;
- 8 **end**

Output: $\hat{\mathcal{L}} \in \mathbb{R}^{n_1 \times \dots \times n_d}$.

where λ_1 and λ_2 are the regularization parameter, \mathcal{L} is an underlying tensor, \mathcal{S} represents sparse noise, and

$$\hat{q}_k = \text{sign}(\langle \mathcal{P}_k, \mathcal{L} + \mathcal{S} \rangle + \epsilon_k + \xi_k),$$

in which the definitions of $\mathcal{P}_k, \epsilon_k$, and ξ_k are similar to those of Model (29). In this paper, Model (29) and Model (30) are named as *generalized nonconvex OBHTC* (GNOBHTC) and *generalized nonconvex OBRHTC* (GNOBRHTC), respectively.

2) **Optimization Algorithm:** To facilitate problem-solving, we start by introducing auxiliary variables to equivalently reshape model (29) as

$$\begin{aligned} \min_{\mathcal{L}, \mathcal{Z}, \mathcal{G}_i} & \frac{1}{2m} \sum_{k=1}^m (\langle \mathcal{P}_k, \mathcal{L} \rangle - \theta q_k)^2 + \frac{\lambda}{\gamma} \sum_{i \in \Gamma} \|\mathcal{G}_i\|_{\Phi, \mathcal{L}} + \mathbb{I}_{\{\|\mathcal{L}\|_\infty \leq \alpha\}}, \\ \text{s.t. } & \mathcal{Z} = \mathcal{L}, \mathcal{G}_i = \nabla_i(\mathcal{Z}), i \in \Gamma, \end{aligned} \quad (31)$$

where the indicator function $\mathbb{I}_{\{\|\mathcal{L}\|_\infty \leq \alpha\}}$ is such that: 1) $\mathbb{I}_{\{\|\mathcal{L}\|_\infty \leq \alpha\}} = 0$, if $\|\mathcal{L}\|_\infty \leq \alpha$; 2) $\mathbb{I}_{\{\|\mathcal{L}\|_\infty > \alpha\}} = +\infty$, if $\|\mathcal{L}\|_\infty > \alpha$. The ADMM framework is utilized to optimize formula (31), and the iteration procedure is briefly summarized in Algorithm 6. Specifically,

$$\begin{aligned} \mathcal{L}^{(t+1)} = & \mathbf{P}_{\|\mathcal{L}\|_\infty \leq \alpha}[(m\mu^{(t)}\mathcal{Z}^{(t)} + \mathcal{J}_1 - m\mathbf{y}^{(t)}) \\ & \odot (m\mu^{(t)}\mathbf{1} + \mathcal{J}_2)], \end{aligned} \quad (32)$$

$$\mathcal{Z}^{(t+1)} = \mathcal{F}^{-1} \left(\frac{\mathcal{F}(\mathcal{L}^{(t)} + \frac{\mathbf{y}^{(t)}}{\mu^{(t)}}) + \mathcal{T}}{\mathbf{1} + \sum_{i \in \Gamma} \mathcal{F}(\mathcal{D}_i)^H \odot \mathcal{F}(\mathcal{D}_i)} \right), \quad (33)$$

$$\mathcal{G}_i^{(t+1)} = \mathcal{D}_{\Phi, \frac{\lambda}{\gamma\mu^{(t)}}}(\nabla_i(\mathcal{Z}^{(t+1)}) + \frac{\Lambda_i^{(t)}}{\mu^{(t)}}), \quad (34)$$

$$\mathbf{y}^{(t+1)} = \mathbf{y}^{(t)} + \mu^{(t)}(\mathcal{L}^{(t+1)} - \mathcal{Z}^{(t+1)}), \quad (35)$$

$$\Lambda_i^{(t+1)} = \Lambda_i^{(t)} + \mu^{(t)}(\nabla_i(\mathcal{Z}^{(t+1)}) - \mathcal{G}_i^{(t+1)}), \quad (36)$$

$$\mu^{(t+1)} = \min(\mu^{\max}, \vartheta\mu^{(t)}), \quad (37)$$

where $\mathbf{P}_{\|\mathcal{L}\|_\infty \leq \alpha}(\cdot)$ stands for projection operator, \odot is denotes elementwise division, the definition of \mathcal{T} is the same as the formula (21), $\mathcal{D}_{\Phi, \tau}(\cdot, \cdot)$ denotes the GNHTSVT operation (see Algorithm 4). **Due to space constraints of this paper, we have placed the detailed ADMM optimization algorithms for solving Model (29) and Model (30), along with their**

TABLE I: Experimental datasets used for evaluation and their detailed information.

Data-Type	Data-Name	Data-Dimension
Order-3 HSIs [Link1] [Link2] [Link3]	HSI 1: KSC	$512 \times 614 \times 176$
	HSI 2: Pavia	$1096 \times 715 \times 102$
	HSI 3: SZUTreeHSI-R1	$1000 \times 1000 \times 98$
	HSI 4: SZUTreeHSI-R2	$1000 \times 1000 \times 98$
Order-3 MRIs [Link4]	MRI 1: 844-4ch6	$500 \times 651 \times 30$
	MRI 2: 1138-ch8	$559 \times 531 \times 30$
	MRI 3: 849-sax38	$528 \times 704 \times 30$
	MRI 4: 958-sax11	$608 \times 456 \times 30$
	MRI 5: 958-4ch10	$407 \times 608 \times 30$
Order-3 MSIs [Link5]	MSI 1: Cloth	$512 \times 512 \times 31$
	MSI 2: Thread-Spools	$512 \times 512 \times 31$
	MSI 3: Jelly-Beans	$512 \times 512 \times 31$
	MSI 4: Feathers	$512 \times 512 \times 31$
Order-4 CVs [Link6]	CV 1: Akiyo	$288 \times 352 \times 3 \times 300$
	CV 2: Container	$288 \times 352 \times 3 \times 300$
	CV 3: Silent	$288 \times 352 \times 3 \times 300$
	CV 4: Waterfall	$288 \times 352 \times 3 \times 260$
	CV 5: News	$288 \times 352 \times 3 \times 300$
	CV 6: Galleon	$288 \times 352 \times 3 \times 360$
Order-4 MRSIs [Link7] [Link8]	MRSI 1: SPOT-5	$1000 \times 1000 \times 4 \times 13$
	MRSI 2: Landsat-7	$1000 \times 1000 \times 6 \times 11$
	MRSI 3: T22LGN	$1000 \times 1000 \times 4 \times 7$
	MRSI 4: T29RMM	$1000 \times 1000 \times 4 \times 6$
Order-5 LFI [Link9]	LFI 1: Mim	$200 \times 300 \times 3 \times 15 \times 15$
	LFI 2: Framed	$200 \times 300 \times 3 \times 15 \times 15$
	LFI 3: Beel	$200 \times 300 \times 3 \times 15 \times 15$
	LFI 4: Bench	$200 \times 300 \times 3 \times 15 \times 15$
	LFI 5: Duck	$200 \times 300 \times 3 \times 15 \times 15$
	LFI 6: Trees2	$200 \times 300 \times 3 \times 15 \times 15$

corresponding time complexity analysis and convergence analysis in the supplementary materials.

VI. EXPERIMENTAL RESULTS

In this section, we perform extensive experiments on both synthetic and real-world tensor data to substantiate the superiority and effectiveness of the proposed approach. Due to the page limitations of this paper, partial synthetic and real experiments are provided in the supplementary material. All the experiments are run on the following two platforms: **1)** Windows 10 and Matlab (R2016a) with an Intel(R) Xeon(R) Gold-5122 3.60GHz CPU and 192GB memory; **2)** Windows 10 and Matlab (R2022b) with an Intel(R) Xeon(R) Gold-6230 2.10GHz CPU and 128GB memory.

Experimental Datasets: In this section, we choose several types of real tensorial data to verify the superiority and effectiveness of the proposed method over compared algorithms. Experimental datasets used for evaluation and their detailed information are summarized in Table I, which cover *multispectral images* (MSIs), *hyperspectral images* (HSIs), *magnetic resonance images* (MRIs), *color videos* (CVs), *multi-temporal remote sensing images* (MRSIs), and *light field images* (LFIs). In our experiments, we normalize the gray-scale value of the tested tensors to the interval $[0, 1]$. For unquantized scenarios, the observed noisy tensor is constructed as follows: the impulse noise with ratio NR is uniformly and randomly added to the ground-truth tensor, and then we sample $(SR \cdot \prod_{i=1}^d n_i)$ pixels from the noisy tensor to form the observed tensor $\mathbf{P}_\Omega(\mathcal{M})$ at random. For quantized scenarios, the sampling rate is defined as $SR = m / \prod_{i=1}^d n_i$, where m denotes the number of samples. The prequantization random noises $\{\epsilon_k\}_{\forall k \in [m]}$ are generated from a mean-zero Gaussian distribution with standard deviation $\sigma > 0$.

Evaluation Metrics: The *Peak Signal-to-Noise Ratio* (PSNR), the *structural similarity* (SSIM), the *relative square error* (RSE), and the CPU time are employed to evaluate the recovery performance. Generally, better recovery performances are reflected by higher PSNR and SSIM values and

lower RSE values. The best and the second-best results are highlighted in red and blue, respectively.

Parameters Setting: Unless otherwise stated, all parameters involved in the competing methods were optimally assigned or selected as suggested in the reference papers. *In the supplementary material, we provide the parameter settings regarding the proposed and compared methods.*

A. Experiments 1: Noise-Free Tensor Completion in Unquantized Tensor Recovery

Competing Algorithms: In this subsection, we compare the proposed GNHTC method and its two randomized versions with a number of state-of-the-art LRTC methods, including TRNN [28], HTNN [29], METNN [31], MTTD [32], WSTNN [30], EMLCP-LRTC [53], TCTV-TC [14], GTNN-HOC [52], and t- ϵ -LogDet [51]. In our randomized versions, one is named R1-GNHTC, integrating the fixed-rank LRTC strategy, while the other is called R2-GNHTC, incorporating the fixed-accuracy LRTC strategy.

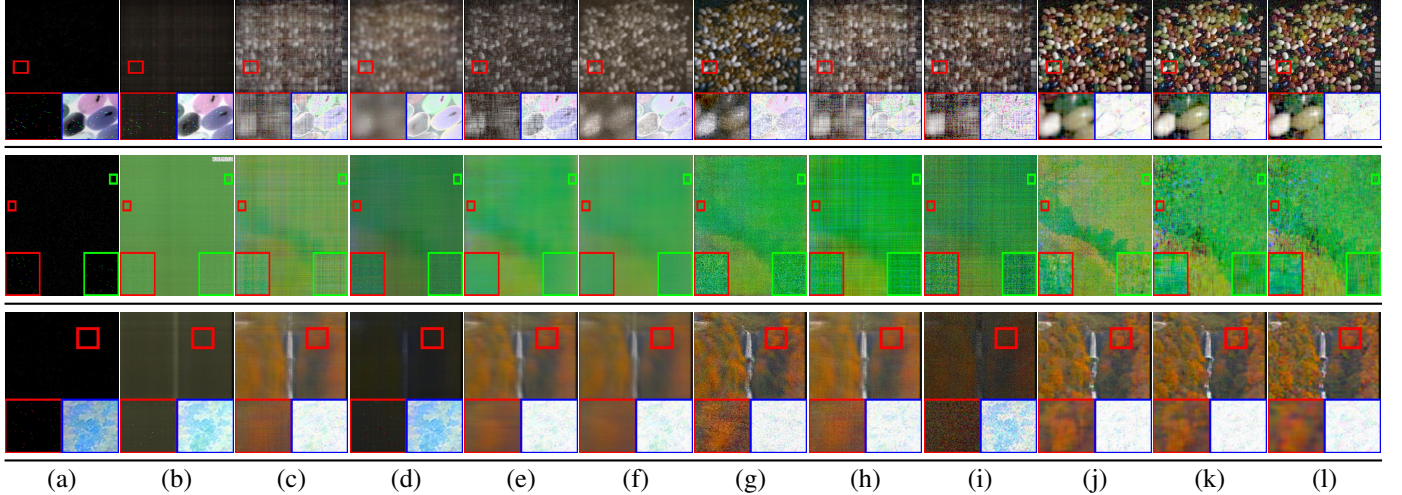
Results and Analysis: Quantitative evaluation results of the proposed and compared LRTC methods on MSIs, MRSIs, and CVs are presented in Table II. These experimental results consistently demonstrate that, especially under extremely low sampling rates, the proposed GNHTC method far surpasses existing high-order LRTC methods, such as HTNN, METNN, MTTD, WSTNN, and EMLCP-LRTC, which purely couple global low-rankness, in terms of the PSNR, SSIM, and RSE metrics. Besides, our deterministic GNHTC algorithm achieves a PSNR gain of approximately 1dB compared to the convex TCTV-TC method. From the perspective of computational efficiency, as the scale of tensor data increases, the gap of CPU Time (Second) between the two proposed randomized algorithms and other deterministic algorithms widens. Notably, when benchmarked against competitive approaches such as METNN, MTTD, WSTNN, EMLCP-LRTC, and TCTV-TC, our randomized algorithms on MRSIs recovery demonstrate a speedup of 5~9 times (3~7 times on CVs). The corresponding visual quality comparisons are provided in Figure 3. This indicates that when other comparison algorithms fail, the proposed method can still restore the general appearance. Since the evaluation metrics obtained by two randomized methods are very similar, we only present the visual results of R1-GNHTC algorithm.

B. Experiments 2: Noisy Tensor Completion in Unquantized Tensor Recovery

Competing Algorithms: We compare the proposed method (GNHTC) and its two accelerated versions with several RLRTC approaches: TRNN [34], TTNN [41], TSPK [39], TTLRR [42], LNOP [54], NRTRM [55], HWTNN [58], HWTNN [16], randomized HWTNN (R-HWTNN) [16], and TCTV-RTC [14]. It is noteworthy that the T-CTV regularizer was solely applied in developing high-order LRTC and TR-PCA models in reference [14]. To highlight the advantages of non-convex regularization over convex regularization within the context of a joint L+S priors strategy, we additionally include the baseline TCTV-RTC model, which can be viewed as a degenerate version of model (15) when $\Phi(\cdot) = \psi(\cdot) = \ell_1$.

TABLE II: Quantitative evaluation of the proposed and compared LRTC methods on MSIs, MRSIs, and CVs.

SR	Evaluation Metric	TRNN [28]	HTNN [29]	METNN [31]	MTTD [32]	WSTNN [30]	EMLCP-LRTC [53]	GTNN-HOC [52]	t- ϵ -LogDet [51]	TCTV-TC [14]	GNHTC	R1-GNHTC	R2-GNHTC
Results on Third-Order MSIs													
SR=1%	MPSNR	14.2487	20.5380	18.4703	21.0184	18.9146	23.4133	20.5633	20.5657	27.4766	28.1947	28.1181	28.0127
	MSSIM	0.3385	0.5129	0.5707	0.5400	0.4903	0.7278	0.4927	0.4926	0.8075	0.8363	0.8243	0.8209
	MRSE	0.9168	0.4460	0.5865	0.4183	0.5727	0.3477	0.4362	0.4474	0.2078	0.1932	0.1946	0.1967
	MTime	720.859	397.523	2030.789	755.391	1670.466	1906.961	465.174	383.452	1444.838	1542.876	535.696	628.513
SR=3%	MPSNR	17.0734	26.3468	25.8454	26.7355	29.4583	29.9045	26.4128	27.2031	31.4842	32.4408	32.0220	31.6791
	MSSIM	0.4950	0.7903	0.8244	0.8066	0.9093	0.9096	0.7930	0.8026	0.9099	0.9316	0.9101	0.8983
	MRSE	0.6506	0.2370	0.2606	0.2217	0.1595	0.1678	0.2299	0.2163	0.1327	0.1195	0.1254	0.1314
	MTime	723.259	350.539	2017.946	713.037	1930.939	1909.037	453.553	349.175	1422.979	1544.423	534.529	626.512
SR=5%	MPSNR	19.8601	28.7757	31.2017	28.9041	32.6543	33.4464	29.7611	30.3920	33.6687	34.6742	34.0703	33.3479
	MSSIM	0.5826	0.8680	0.9275	0.8751	0.9555	0.9501	0.8787	0.8890	0.9420	0.9586	0.9395	0.9200
	MRSE	0.4760	0.1801	0.1389	0.1756	0.1116	0.1188	0.1595	0.1519	0.1045	0.0929	0.0999	0.1100
	MTime	726.038	335.946	2032.377	676.609	1869.232	1908.997	445.278	345.258	1404.638	1540.097	597.850	690.531
Results on Fourth-Order MRSIs													
SR=0.5%	MPSNR	17.2533	19.8339	15.7720	20.9478	20.8181	18.9815	18.3208	16.3231	21.5348	22.7191	22.4954	22.7820
	MSSIM	0.3910	0.4132	0.3557	0.4658	0.4701	0.4772	0.3637	0.3250	0.5359	0.5905	0.5695	0.5771
	MRSE	0.5510	0.3644	0.6399	0.3268	0.3491	0.3974	0.4082	0.5451	0.3161	0.2631	0.2660	0.2586
	MTime	13633.161	2852.105	9833.043	9106.050	20063.516	19070.785	3183.932	3343.147	9196.801	10506.549	1744.389	1870.817
SR=1%	MPSNR	19.9934	21.2452	18.4103	23.0171	22.4238	19.3586	19.7498	18.2973	23.2805	24.3680	24.0644	24.2869
	MSSIM	0.4437	0.4974	0.4292	0.5802	0.5626	0.5358	0.4675	0.4250	0.6388	0.6828	0.6727	0.6773
	MRSE	0.3853	0.3156	0.4714	0.2620	0.2873	0.3758	0.3509	0.4306	0.2564	0.2235	0.2244	0.2194
	MTime	13536.008	2739.258	9861.887	8855.057	20129.556	19136.206	3193.774	3194.831	9231.643	10493.834	1815.473	1992.958
Results on Fourth-Order CVs													
SR=0.5%	MPSNR	12.8418	23.8049	10.6131	24.2577	20.4145	18.7434	22.8838	11.4957	26.2302	26.9312	24.7963	25.3219
	MSSIM	0.4538	0.6208	0.3436	0.6917	0.6270	0.3322	0.4877	0.1129	0.7332	0.7479	0.6766	0.6829
	MRSE	0.5543	0.1588	0.7079	0.1520	0.2268	0.2721	0.1747	0.6254	0.1187	0.1101	0.1399	0.1314
	MTime	8884.572	5589.675	13830.999	16389.214	30441.946	31394.932	5838.133	6139.929	11029.124	12837.645	3002.928	3481.961
SR=1%	MPSNR	17.9342	25.9737	12.5734	26.0504	26.2277	25.9325	24.7281	13.9930	28.3663	28.7626	26.0067	26.3973
	MSSIM	0.5492	0.6971	0.4150	0.7449	0.7526	0.6601	0.5665	0.1717	0.7929	0.7994	0.7087	0.7155
	MRSE	0.3138	0.1254	0.5735	0.1246	0.1232	0.1275	0.1420	0.4703	0.0941	0.0906	0.1219	0.1164
	MTime	8900.368	5528.504	13871.996	16361.459	30502.989	31443.264	5802.668	6135.755	11073.196	12629.969	3293.247	4008.781

Fig. 3: Visual comparison of various LRTC methods on MSIs (top, SR=1%), MRIs (middle, SR=1%), and CVs (bottom, SR=0.5%). From left to right: (a) Observed, (b) TRNN, (c) HTNN, (d) METNN, (e) MTTD, (f) WSTNN, (g) EMLCP-LRTC, (h) GTNN-HOC, (i) t- ϵ -LogDet, (j) TCTV-TC, (k) GNHTC, (l) R1-GNHTC.

In our proposed randomized algorithms, the versions coupled with fixed-rank and fixed-accuracy LRTA strategies are named R1-GNRHTC and R2-GNRHTC, respectively. Since the evaluation metrics obtained by two randomized methods are very similar, we only present the visual results of R1-GNRHTC algorithm.

1) Results and Analysis on Third-Order HSIs and MRIs datasets: In term of quantitative evaluation indicators (e.g., average PSNR, SSIM, RSE and CPU Time), Table III reports the restoration results of various RLRTC methods on MRIs datasets and HSIs datasets. From these results, we can observe that: **1)** In comparison to other compared algorithms, some of which rely solely on global low-rankness, TCTV-RTC and GNRHTC exhibit superior recovery performance by integrating both global low-rank and local smoothness priors; **2)** The proposed GNRHTC method gains approximately 1-2 dB in PSNR over the convex TCTV-RTC method, demonstrating the advantage of nonconvex regularization scheme in high-order

tensor modeling; **3)** For the proposed RLRTC method, while incurring a slight loss in accuracy, the version embedding randomized techniques significantly enhances computational efficiency compared to its deterministic counterpart. In other words, the randomized GNRHTC is approximately 3-4 times faster than the deterministic version across various sampling rates and impulse noise ratios. Some inpainting examples concerning MRI and HSI datasets are depicted in Figure 4 and 5, respectively. Compared to other popular peers, the proposed method is able to recover more distinct detail and contour information, which is especially evident in low-sampling scenarios (e.g., 1% and 5%).

2) Results and Analysis on Fourth-Order MRSIs and CVs, and Fifth-Order LFIs: In Tables IV, we summarize the mean PSNR, RSE, SSIM values and CPU time of different RLRTC methods for MRSIs, CVs, and LFIs, where $SR = 0.1, 0.2, NR = 1/3, 0.5$. Figures 6 and 7 present the visual comparisons of the enlarged areas in restored CVs, LFIs, and MRSIs,

TABLE III: Quantitative evaluation PSNR, SSIM, RSE and CPU Time (Second) of the proposed and compared RLRTC methods on third-order HSI and MRI datasets.

SR & NR	Evaluation Metric	TTNN [41]	TSPK [39]	TTLRR [42]	LNOP [54]	NRTRM [55]	HWTNN [58]	HWTSN [16]	R-HWTSN [16]	TCTV-RTC [14]	GNRHTC	R1-GNRHTC	R2-GNRHTC
<i>Results on Third-Order MRIs</i>													
SR=0.1 & NR= 0.5	MPSNR	23.8409	22.7573	24.4542	23.8835	24.6133	25.9725	26.9158	27.0206	30.4559	31.5027	31.2989	30.9439
	MSSIM	0.7115	0.6461	0.5349	0.5235	0.7222	0.6353	0.7327	0.7615	0.8972	0.9039	0.8967	0.9222
	MRSE	0.2305	0.2619	0.2112	0.2340	0.2116	0.1860	0.1683	0.1658	0.1076	0.0954	0.0978	0.1019
	MTime	255.368	420.435	509.757	324.997	323.459	366.837	471.374	174.369	851.556	991.191	257.378	287.212
SR=0.05 & NR=0.5	MPSNR	20.4528	19.8246	20.4787	19.8633	20.4842	22.6056	22.7329	22.5098	26.5574	28.0649	27.9266	27.8158
	MSSIM	0.5547	0.4519	0.3377	0.2569	0.6274	0.5204	0.5750	0.5757	0.8152	0.8362	0.8167	0.8478
	MRSE	0.3379	0.3621	0.3322	0.3623	0.3370	0.2634	0.2668	0.2736	0.1669	0.1410	0.1434	0.1455
	MTime	278.546	420.158	522.046	320.049	323.467	364.056	452.823	164.333	831.944	988.753	238.458	269.629
<i>Results on Third-Order HSI</i>													
SR=0.05 & NR=0.5	MPSNR	22.6243	22.1360	23.3060	22.8259	22.5062	22.9506	24.5271	23.4906	27.9127	28.7180	26.7984	26.3515
	MSSIM	0.5534	0.4655	0.4767	0.4402	0.6070	0.5504	0.5651	0.5645	0.7752	0.8166	0.7089	0.6960
	MRSE	0.4057	0.4278	0.3724	0.3962	0.4122	0.3934	0.3271	0.3693	0.2216	0.2068	0.2540	0.2674
	MTime	3554.179	6127.126	6956.448	4962.299	4841.568	4022.126	4987.924	1998.454	8635.938	10778.794	2735.866	2990.031
SR=0.01 & NR=0.5	MPSNR	19.4161	18.7400	18.3855	17.1151	19.1376	17.1177	17.3052	17.2905	22.9375	23.1347	22.5751	23.0700
	MSSIM	0.4237	0.3595	0.2508	0.4554	0.4230	0.3011	0.2752	0.2740	0.5295	0.5456	0.4101	0.5443
	MRSE	0.5829	0.6303	0.6563	0.7597	0.6019	0.7600	0.7439	0.7450	0.3895	0.3835	0.4056	0.3864
	MTime	3608.7448	5997.314	7336.936	4641.734	4631.646	3939.969	4675.494	1683.462	9034.219	10656.386	2676.158	2844.831

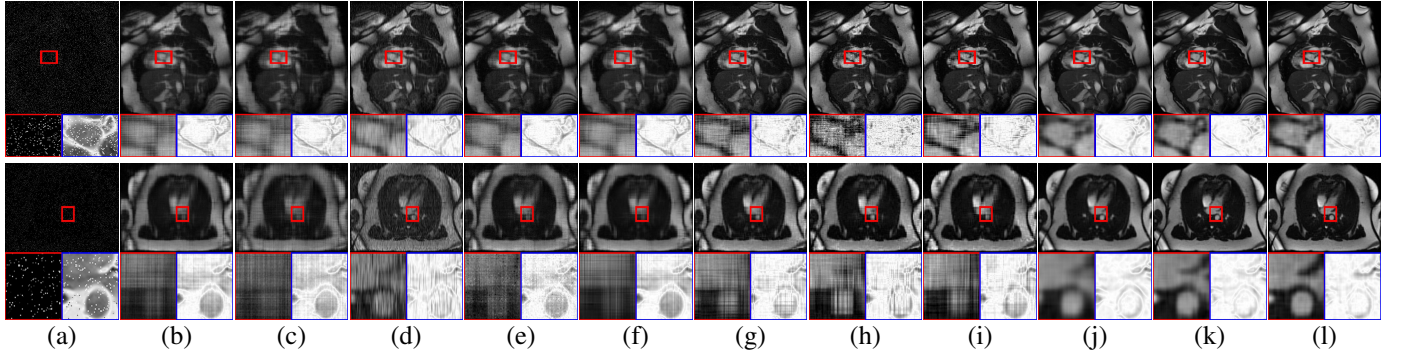
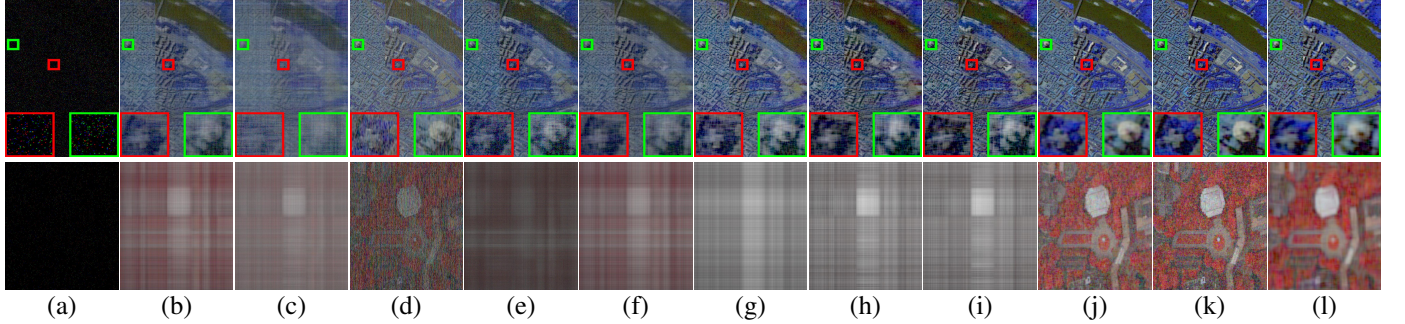
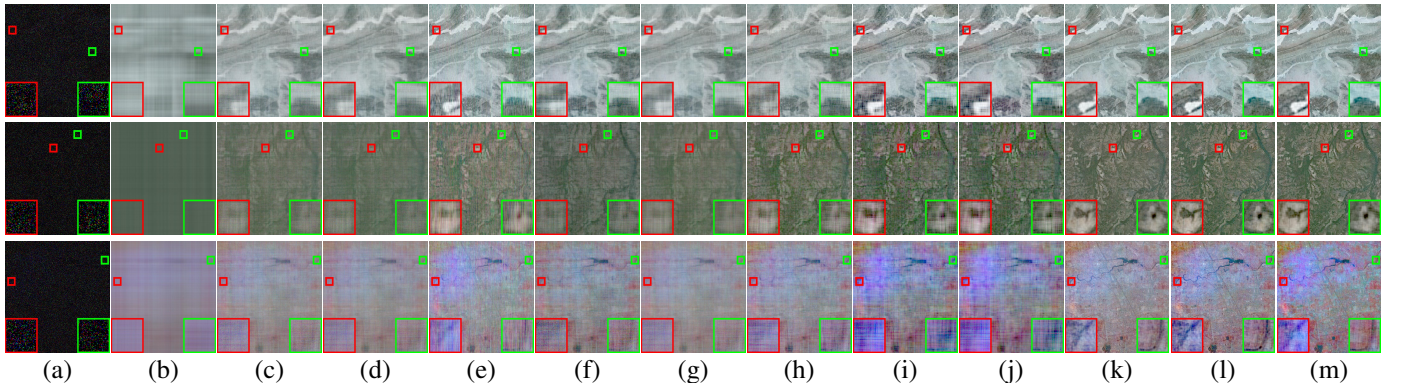
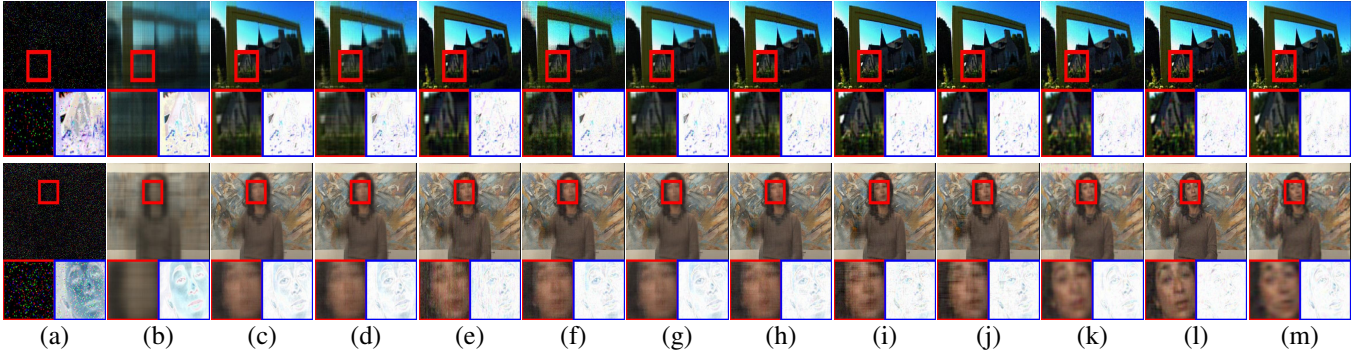
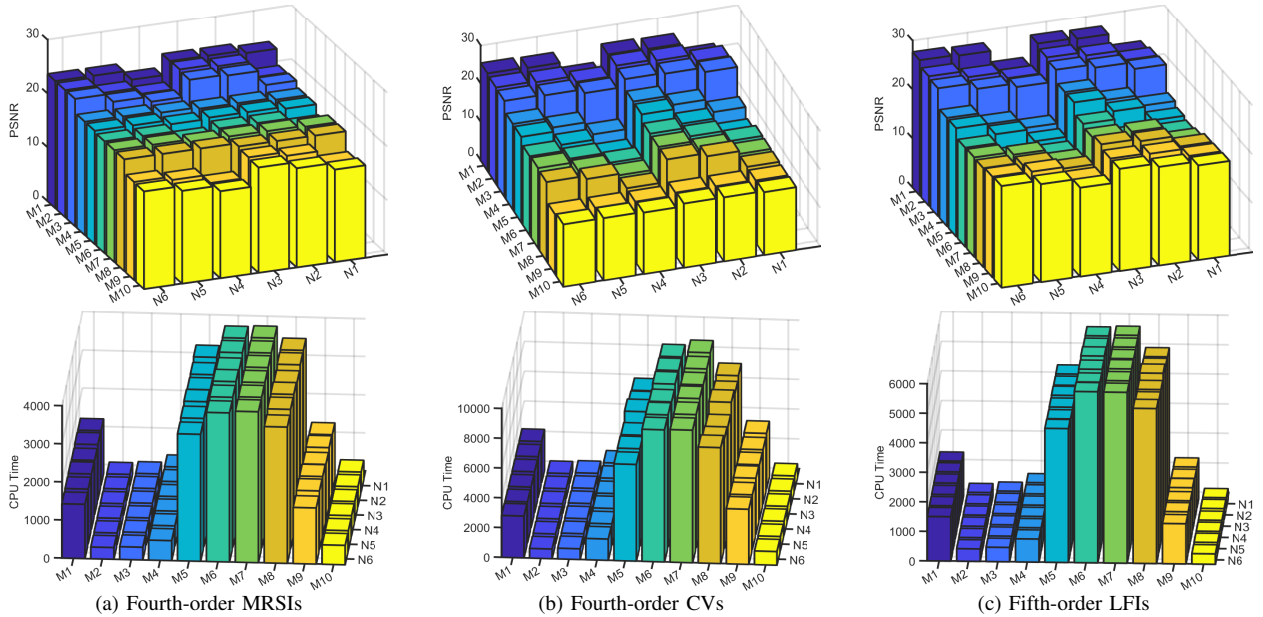
Fig. 4: Visual comparison of various RLRTC methods for MRI datasets inpainting. From top to bottom, the parameter pair (SR, NR) are $(0.1, 0.5)$ and $(0.05, 0.5)$, respectively. From left to right: (a) Observed, (b) TTNN, (c) TSPK, (d) TTLRR, (e) LNOP, (f) NRTRM, (g) HWTNN, (h) HWTSN, (i) R-HWTSN, (j) TCTV-RTC, (k) GNRHTC, (l) R1-GNRHTC.Fig. 5: Visual comparison of various RLRTC methods for HSI datasets recovery. From top to bottom, the parameter pair (SR, NR) are $(0.05, 0.5)$ and $(0.01, 0.5)$, respectively. From left to right: (a) Observed, (b) TTNN, (c) TSPK, (d) TTLRR, (e) LNOP, (f) NRTRM, (g) HWTNN, (h) HWTSN, (i) R-HWTSN, (j) TCTV-RTC, (k) GNRHTC, (l) R-GNRHTC.Fig. 6: Visual comparison of various RLRTC methods for MRSIs inpainting under $(SR, NR) = (0.1, 0.5)$. From left to right: (a) Observed, (b) TRNN, (c) TTNN, (d) TSPK, (e) TTLRR, (f) LNOP, (g) NRTRM, (h) HWTNN, (i) HWTSN, (j) R-HWTSN, (k) TCTV-RTC, (l) GNRHTC, (m) R-GNRHTC.

TABLE IV: Quantitative evaluation PSNR, SSIM, RSE, CPU Time (Second) of the proposed and compared RLRTC methods on fourth-order MRSIs and CVs, and fifth-order LFIs.

SR & NR	Evaluation Metric	TRNN [34]	TTNN [41]	TSPK [39]	TTLRR [42]	LNOP [54]	NRTRM [55]	HWTNN [58]	HWTSN [16]	R-HWTSN [16]	TCTV-RTC [14]	GNRHTC	R1-GNRHTC	R2-GNRHTC
Results on Fourth-Order MRSIs														
SR=0.1 & NR=1/3	MPSNR	20.8668	23.5098	23.5289	23.9632	23.8890	23.6531	23.9005	24.0602	23.9741	26.0960	26.3349	26.3656	26.3597
	MSSIM	0.4904	0.5281	0.5283	0.4840	0.4909	0.5482	0.4931	0.5064	0.5002	0.6553	0.6496	0.6202	0.6203
	MRSE	0.3387	0.2711	0.2687	0.2398	0.2518	0.2684	0.2518	0.2473	0.2476	0.2171	0.2092	0.1839	0.1842
	MTime	3942.46	1719.65	3176.77	3550.68	2213.47	2113.38	1994.28	2654.98	1194.43	4108.24	5428.79	1340.78	1708.39
SR=0.1 & NR=0.5	MPSNR	19.7638	22.1445	22.0155	21.3846	21.8048	22.5362	22.3005	22.1249	22.0964	24.3981	24.3911	24.9018	24.9179
	MSSIM	0.4724	0.4208	0.4306	0.3155	0.4141	0.4767	0.4042	0.3994	0.4069	0.5804	0.5851	0.5555	0.5588
	MRSE	0.3802	0.3121	0.3176	0.2884	0.3380	0.3051	0.3003	0.2963	0.2990	0.2644	0.2627	0.2214	0.2212
	MTime	3967.29	1731.32	3207.05	3482.18	2268.15	2118.69	1982.67	2636.47	1203.59	4010.51	5398.73	1347.37	1675.08
Results on Fourth-Order CVs														
SR=0.1 & NR=1/3	MPSNR	21.6719	27.2999	27.3469	28.4580	28.4289	27.9123	28.9986	30.1071	27.5967	29.3515	31.0519	28.6433	28.3286
	MSSIM	0.6877	0.8505	0.8983	0.8397	0.8301	0.8626	0.8644	0.8833	0.8112	0.8589	0.9123	0.8159	0.8110
	MRSE	0.1850	0.0977	0.0908	0.0859	0.0858	0.0912	0.0811	0.0725	0.0950	0.0785	0.0627	0.0859	0.0889
	MTime	3048.46	2251.99	3755.75	5999.45	2930.37	2530.27	2768.61	3413.39	1874.28	4653.09	6200.28	1755.31	2160.53
SR=0.1 & NR=0.5	MPSNR	19.0174	25.7810	26.0552	26.7229	25.7733	26.4971	26.8800	27.9984	26.0465	26.3012	28.8414	26.8368	26.2677
	MSSIM	0.5966	0.8114	0.8651	0.7248	0.7673	0.8265	0.8133	0.8315	0.7708	0.7737	0.8534	0.7708	0.7534
	MRSE	0.2503	0.1157	0.1049	0.1056	0.1161	0.1071	0.1029	0.0916	0.1122	0.1107	0.0804	0.1053	0.1124
	MTime	2920.95	2393.36	3662.44	5922.98	2982.35	2569.06	2726.56	3390.48	1871.82	4461.77	6257.18	1576.33	1732.92
Results on Fifth-Order LFIs														
SR=0.05 & NR=1/3	MPSNR	19.5675	27.7763	25.4831	28.7039	25.8129	28.5711	28.3114	30.1991	28.6890	29.9660	30.7448	27.3391	26.7011
	MSSIM	0.6088	0.8842	0.8359	0.8869	0.7319	0.9076	0.8794	0.8624	0.8730	0.9032	0.9239	0.8416	0.8294
	MRSE	0.3299	0.1295	0.1677	0.1154	0.1606	0.1184	0.1227	0.1003	0.1187	0.1029	0.0940	0.1393	0.1492
	MTime	3132.39	1765.27	3293.65	3932.82	2600.87	2078.55	2142.27	2325.07	1326.56	2931.57	3630.29	1011.59	1200.67
SR=0.05 & NR=0.5	MPSNR	17.0493	24.5345	22.7260	25.4637	19.7810	25.1724	25.3275	26.8663	26.3289	25.1870	27.8194	27.2358	26.9874
	MSSIM	0.5350	0.8069	0.7037	0.7735	0.5272	0.8275	0.7595	0.8332	0.8076	0.7837	0.8668	0.7941	0.7859
	MRSE	0.4365	0.1874	0.2293	0.1715	0.3243	0.1740	0.1715	0.1461	0.1553	0.1771	0.1277	0.1398	0.1434
	MTime	3168.99	1838.05	3219.03	3780.72	2645.66	2085.77	2131.19	2334.08	1319.79	2851.29	3531.73	997.29	1174.51

Fig. 7: Visual comparison of various RLRTC methods for CVs/LFIs inpainting under $(SR, NR) = (0.05, 0.5)$ and $(SR, NR) = (0.1, 0.5)$, respectively. From left to right: (a) Observed, (b) TRNN, (c) TTNN, (d) TSPK, (e) TTLRR, (f) LNOP, (g) NRTRM, (h) HWTNN, (i) HWTSN, (j) R-HWTSN, (k) TCTV-RTC, (l) GNRHTC, (m) R-GNRHTC.Fig. 8: The recovery performance of the proposed and compared OBTC under various sampling rates and Gaussian noise levels. **M1:** GNOBHTC, **M2:** R1-GNOBHTC, **M3:** R2-GNOBHTC, **M4:** 1BRTC [37], **M5:** MLE-TNN [111], **M6:** MLE-Max [112], **M7:** MLE-Factor [112], **M8:** MLE-T2M [113], **M9:** MLE-Mat [114], **M10:** L2-Mat [83]. **N1:** $SR = 0.1, \sigma = 0$, **N2:** $SR = 0.3, \sigma = 0$, **N3:** $SR = 0.5, \sigma = 0$, **N4:** $SR = 0.1, \sigma = 0.2$, **N5:** $SR = 0.3, \sigma = 0.2$, **N6:** $SR = 0.5, \sigma = 0.2$.

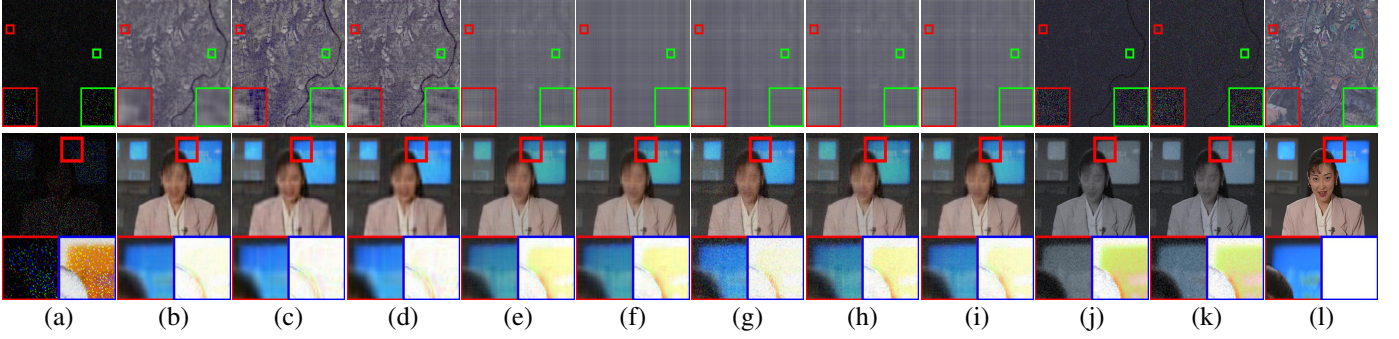


Fig. 9: Visual comparison of various OBTC methods for CVs and MRSIs datasets recovery. The observed CVs and MRSIs are corrupted by noises generated from Gaussian distribution with mean zero and standard deviation $\sigma = 0.2$, and the sampling rates is set to be 0.1 (CVs), 0.3 (MRSIs). From left to right: (a) Observed, (b) GNOBHTC, (c) R1-GNOBHTC, (d) R2-GNOBHTC, (e) 1BRTC, (f) MLE-TNN, (g) MLE-Max, (h) MLE-Factor, (i) MLE-T2M, (j) L2-Mat, (k) MLE-Mat, (l) Ground-truth.

which were obtained through various RLRTC methods. The conclusions from the robust restoration of MRSIs mirror those of third-order MRIs and HSIs. Namely, our method continues to exhibit a notable superiority over other competing peers. In particular, at low sampling rates and high noise levels, the RLRTC models that purely rely on \mathbf{L} prior fail to reconstruct missing and noisy tensor data well, whereas our proposed method performs oppositely. Although the gap between the proposed method and those purely using \mathbf{L} prior in CVs/LFIs restoration is not as extremely pronounced as that observed in the first three tensor recovery scenarios, it still demonstrates good performance in terms of visual quality and quantitative outcomes. Compared with the highly competitive TCTV-RTC and HWTSN algorithms, the improvements of the proposed GNRHTC method are around 2 dB in terms of PSNR values. In addition, among all nonconvex RLRTC methods, our randomized approach achieves the shortest CUP running time.

C. Experiments 3: One-Bit Tensor Completion in Quantized Tensor Recovery

In this subsection, we compare the proposed GNOBHTC method and its two randomized versions with some state-of-the-art *one-bit tensor completion* (OBTC) approaches, including MLE-Mat [114], L2-Mat [83], MLE-TNN [111], MLE-T2M [113], MLE-Max [112], MLE-Factor [112], and 1BRTC [37]. Two randomized versions, which integrate the fixed-rank and fixed-accuracy LRTC strategies, are named as R1-GNOBHTC and R2-GNOBHTC, respectively.

Under varying sampling rates and noise levels, Figure 8 presents the quantitative results (including CPU time and PSNR) of the proposed and comparative OBTC methods evaluated on LFIs, CVs, and MRSIs datasets. The corresponding visual comparisons are provided in Figure 9. Similarly to the aforementioned non-quantized tensor recovery, the proposed deterministic GNOBHTC method achieves higher PSNR values than all competing algorithms. Additionally, the proposed randomized algorithms demonstrate the lowest computational cost among all evaluated methods. This validates the advantages of the proposed nonconvex tensor modeling, $\mathbf{L}+\mathbf{S}$ priors-based representation paradigm, and randomized strategies in quantized tensor recovery.

D. Related Discussions

In this subsection, under various types of real-world tensors with different sampling rates and impulse noise levels, we mainly focus on the following key experiments to illustrate our research motivations:

- **Experiment 1:** analyze the performance of various non-convex regularizers $\Phi(\cdot)+\psi(\cdot)$ on our proposed deterministic and randomized recovery algorithms, respectively;
- **Experiment 2:** analyze how different prior structures (i.e., $\mathbf{L}+\mathbf{S}$ priors and pure \mathbf{L} prior) influence the recovery performance of our proposed recovery algorithm in deterministic and randomized patterns, respectively;
- **Experiment 3:** investigate the influence of various fixed-rank randomized Tucker compression methods upon restoration results of our proposed randomized recovery algorithm under different target rank $\mathbf{r} = (r_1, \dots, r_d)$;
- **Experiment 4:** investigate the influence of various fixed-precision randomized Tucker compression approaches upon restoration results of our proposed randomized recovery algorithm under different block size b ;

Wherein, the test tensor data are HSIs, MRI datasets, CVs, MRSIs and LFIs (please see Table 1 for details).

1) Results and Analysis of Experiments 1-2: Note that $\Phi(\cdot)$ and $\psi(\cdot)$ could be the same. The nonconvex regularization penalties in our experiments include firm, SCAD, MCP, Log, ℓ_q , weighted- ℓ_q and capped- ℓ_q , where $\Phi(\cdot)$ and $\psi(\cdot)$ are the same nonconvex functions in each case, namely MCP+MCP (N1), SCAD+SCAD (N2), weighted- ℓ_q +weighted- ℓ_q (N3), For different $\Phi(\cdot)$ and $\psi(\cdot)$, we test ten cases: capped- ℓ_q + ℓ_q (N4), capped- ℓ_q +MCP (N5), capped- ℓ_q +SCAD (N6), Log+ ℓ_q (N7), Log+MCP (N8), Log+SCAD (N9), ℓ_q +MCP (N10), ℓ_q +SCAD (N11), MCP+ ℓ_q (N12), SCAD+ ℓ_q (N13). To illustrate the advantages of nonconvex methods, we also include the basic convex scenario for comparison, i.e., ℓ_1 + ℓ_1 (N14). We set (SR, NR) to be (0.1, 1/3) (C1), (0.2, 1/3) (C2), (0.3, 1/3) (C3), (0.5, 1/3) (C4), (0.1, 0.5) (C5), (0.2, 0.5) (C6), (0.3, 0.5) (C7), (0.5, 0.5) (C8). For the noise/outliers regularization item, $h(\cdot) = \|\cdot\|_{\ell_1}$ is defined as the ℓ_1 -norm. In this experiment, we set $\vartheta = 1.1$, $\varpi = 10^{-4}$, $\mathcal{L} = \text{FFT}$, $\mu^{\{0\}} = 10^{-3}$, $\mu^{\max} = 10^{10}$; $\Gamma = \{1, 2, 3\}$ (HSIs), $\Gamma = \{1, 2, 4\}$ (CVs), $\Gamma = \{1, 2, 4, 5\}$ (LFIs); $\lambda = \xi / (\max(n_1, n_2) \cdot \prod_{i=3}^d n_i)^{1/2}$, $\xi \in \{2, 3, 4, 5, 6, 8, 10, 12, 15, 18\}$ (N3),

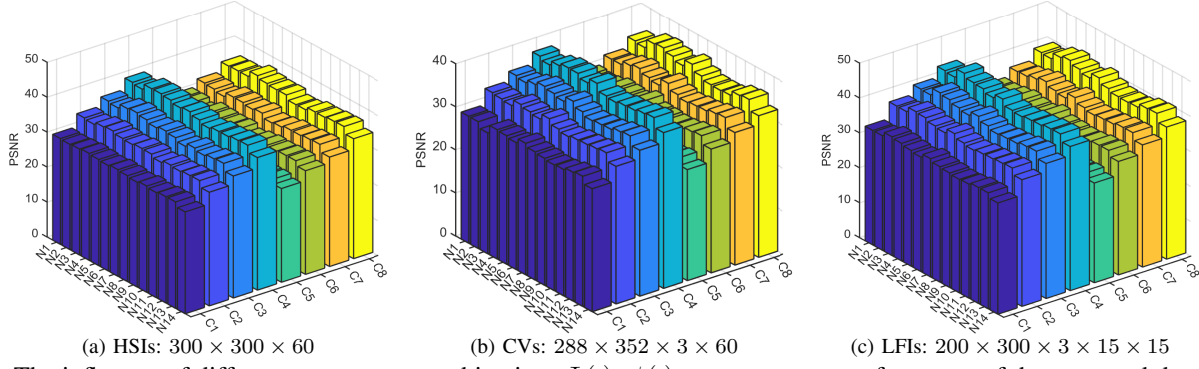


Fig. 10: The influence of different nonconvex combinations $\Phi(\cdot) + \psi(\cdot)$ upon recovery performance of the proposed deterministic GNRHTC algorithm under various sampling rates SR and impulse noise levels NR .

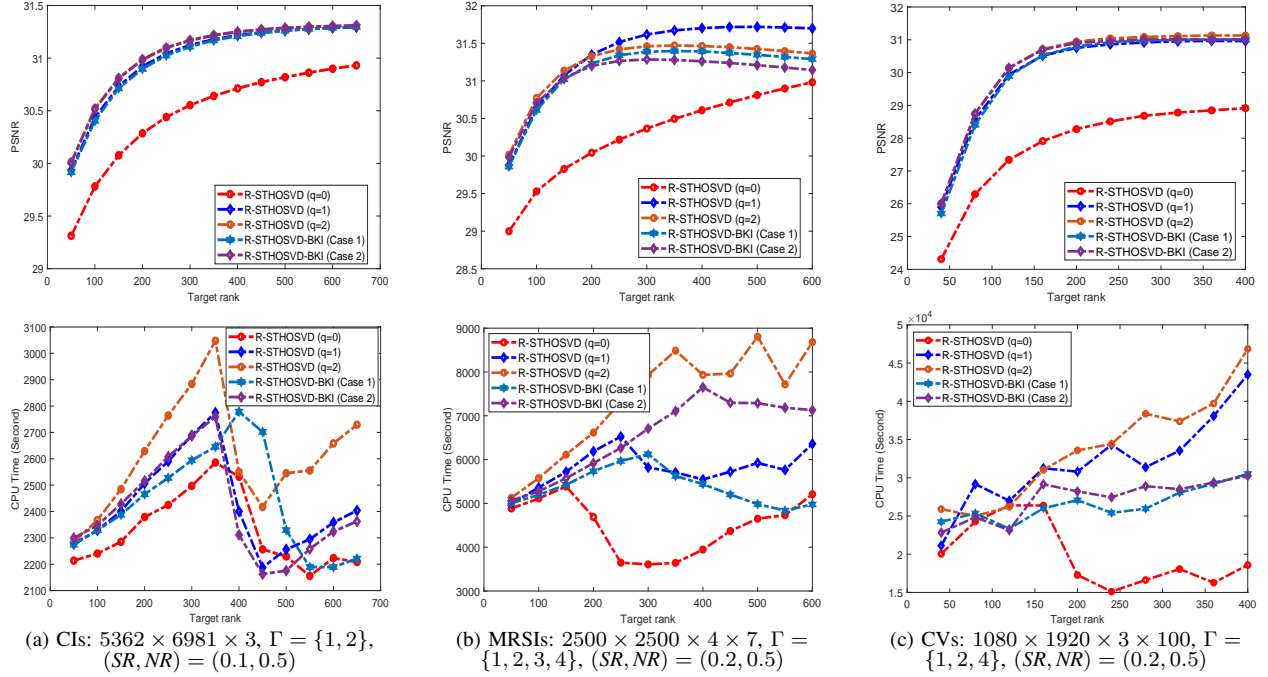


Fig. 11: The influence of various fixed-rank LRTA methods upon restoration performance of the proposed randomized GNRHTC algorithm under different target rank $r = (r_1, \dots, r_d)$. In the proposed algorithm, set $q = [4, 4, *]$, $q = [4, 4, *, *]$, or $q = [4, 4, *, 4]$, $b = \lceil r./4 \rceil$ (Case 1), $b = \lceil r./3 \rceil$ (Case 2). An asterisk indicates that compression is not applied to this mode.

TABLE V: Quantitative evaluation of our deterministic and randomized methods on large-scale CIs, CVs, LFIs and MRSIs. In each method, the values listed from top to bottom represent the PSNR, SSIM, RSE and CPU Time (Minute), respectively.

Data-Type	CIs				HSIs				MRSIs				CVs				Average Value
SR	0.1		0.2		0.1		0.05		0.2		0.1		0.1		0.2		
NR	1/3	0.5	1/3	0.5	1/3	0.5	1/3	0.5	1/3	0.5	1/3	0.5	1/3	0.5	1/3	0.5	
GNRHTC (N1)	33.099	30.929	35.207	34.082	31.285	29.935	28.632	27.633	32.998	31.636	31.000	30.212	31.299	29.361	34.598	32.035	31.496
	0.8165	0.7895	0.8600	0.8362	0.9055	0.8699	0.8310	0.7862	0.8274	0.7993	0.7847	0.7643	0.9031	0.8400	0.9220	0.9090	0.8402
	0.0458	0.0585	0.0357	0.0406	0.1339	0.1570	0.1817	0.2038	0.1571	0.1777	0.1927	0.2183	0.0740	0.0924	0.0506	0.0680	0.1179
	336.15	321.40	321.69	332.80	197.09	198.36	197.63	190.63	604.82	616.95	603.99	603.58	478.06	485.95	481.86	481.69	403.29
R1-GNRHTC (N1)	33.045	31.155	34.947	34.088	28.458	27.952	27.095	26.517	33.892	32.362	31.947	29.972	34.791	31.257	37.996	35.451	31.932
	0.8147	0.7916	0.8515	0.8331	0.8043	0.7917	0.7613	0.7399	0.8325	0.8013	0.7841	0.7567	0.9199	0.8701	0.9370	0.9162	0.8253
	0.0460	0.0571	0.0368	0.0406	0.1854	0.1965	0.2169	0.2318	0.1231	0.1479	0.1545	0.2207	0.0495	0.0747	0.0342	0.0458	0.1163
	35.024	37.71	41.04	38.96	71.01	71.27	68.19	68.37	132.22	132.34	118.43	91.22	121.09	111.22	141.05	144.67	88.98
R2-GNRHTC (N1)	33.026	31.187	34.875	34.054	28.078	27.652	26.894	26.314	33.377	32.097	31.677	29.837	34.377	31.937	37.578	35.887	31.802
	0.8140	0.7919	0.8491	0.8318	0.7909	0.7808	0.7511	0.7325	0.8189	0.7947	0.7789	0.7535	0.9176	0.8915	0.9347	0.9243	0.8222
	0.0462	0.0569	0.0371	0.0407	0.1937	0.2239	0.2034	0.2373	0.1280	0.1511	0.1573	0.2236	0.0519	0.0687	0.0359	0.0436	0.1187
	40.28	49.65	59.54	59.48	81.18	81.02	75.91	75.35	141.64	138.16	124.11	119.44	139.74	142.88	168.67	167.72	104.04
GNRHTC (N4)	33.385	28.649	34.723	30.799	33.733	30.768	30.324	28.279	34.388	31.335	31.569	30.298	32.469	30.038	35.682	33.286	31.857
	0.8150	0.6988	0.8378	0.7017	0.9070	0.8319	0.8664	0.7837	0.8565	0.7628	0.7804	0.7389	0.8674	0.8635	0.9102	0.8625	0.8177
	0.0442	0.0761	0.0378	0.0597	0.1010	0.1421	0.1496	0.1892	0.1198	0.1511	0.1651	0.1899	0.0646	0.0855	0.0446	0.0589	0.1049
	386.81	389.52	396.27	387.06	233.95	238.29	241.17	240.20	604.69	609.97	626.33	636.66	587.03	584.53	579.18	579.06	457.54
R1-GNRHTC (N4)	33.558	29.501	35.336	33.468	28.989	28.394	27.534	26.742	34.286	32.628	32.163	30.127	35.396	30.942	38.488	36.789	32.146
	0.8199	0.7363	0.8570	0.8065	0.8169	0.8077	0.7756	0.7545	0.8337	0.7896	0.7699	0.7432	0.9132	0.8511	0.9319	0.9228	0.8206
	0.0433	0.0690	0.0351	0.0436	0.1744	0.1868	0.2062	0.2259	0.1121	0.1348	0.1408	0.1975	0.0461	0.0770	0.0323	0.0393	0.1102
	53.33	45.51	62.27	59.07	68.66	69.58	65.38	64.95	130.89	132.66	116.46	116.83	138.85	125.57	174.22	149.16	98.33
R2-GNRHTC (N4)	33.594	29.692	35.257	33.692	28.525	28.192	27.754	26.573	33.973	32.721	32.259	30.030	35.297	30.876	38.273	34.865	31.973
	0.8205	0.7440	0.8545	0.8129	0.8033	0.7955	0.7639	0.7461	0.8267	0.7955	0.7766	0.7420	0.9171	0.8571	0.9334	0.9032	0.8182
	0.0431	0.0675	0.0355	0.0425	0.1839	0.1950	0.2149	0.2321	0.1139	0.1337	0.1399	0.1991	0.0467	0.0776	0.0331	0.0490	0.1129
	72.83	73.81	76.47	69.27	79.05	80.2985	72.80	71.93	144.01	124.25	142.01	119.84	148.21	148.83	185.19	186.93	112.23

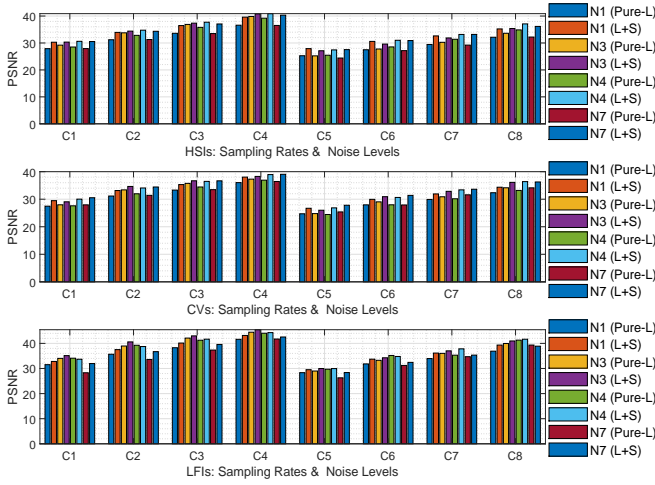


Fig. 12: The influence of different prior structures (i.e., L+S priors and pure L prior) upon recovery performance of the proposed GNRHTC algorithm under various sampling rates SR and impulse noise levels NR .

$\xi \in \{4, 6, 8, 10, 12, 14, 16, 18, 20, 25, 30, 35\}$ (**N7-N9**), $\xi \in \{0.5, 0.8, 1, 1.2, 1.5, 1.8, 2, 2.2, 2.5, 3, 3.5, 4, 4.5, 5\}$ (**Others**).

To enhance computational efficiency, we have scaled down the original HSIs and CVs to a certain extent. The relevant results of **Experiment 1** are displayed in Figure 10, from which it can be seen that the N3, N4 and N7 combinations can achieve relatively better recovered results than other non-convex combinations in most cases. Additionally, the PSNR values obtained with the basic combination N14 are lower than those obtained with other combinations, indicating an advantage of nonconvex regularization over convex regularization in the high-order tensor recovery problem. The results of **Experiment 2** are given in Figure 12, which demonstrate that the GNRHTC method modeled by joint L+S priors consistently outperforms the approach that solely utilizes the L prior under different nonconvex combinations $\Phi(\cdot)+\psi(\cdot)$. Collectively, these results imply that the integration of the L+S prior strategy with nonconvex regularization for the tensor recovery problem is both effective and advantageous.

Table V showcases a performance comparison between the deterministic and randomized versions of the proposed GNRHTC method across different nonconvex functions. This experiment is tested on multiple visual large-scale tensor datasets, i.e., a color image (CI): $5362 \times 6981 \times 3$, a HSI dataset: $1000 \times 1000 \times 98$, a MRSI dataset: $2000 \times 2000 \times 4 \times 7$, and a CV dataset: $1080 \times 1920 \times 3 \times 50$. We can observe that with a slight loss in accuracy or comparable accuracy levels maintained, the version incorporating randomized techniques shows a substantial reduction in computational cost compared to its deterministic counterpart. This result indicates that incorporating the randomized LRTA strategy into tensor recovery problem can overcome computational bottlenecks, particularly for large-scale high-order tensor data.

In above-mentioned large-scale experiment, we set $\mu^{\{0\}} = 10^{-3}$, $\mu^{\max} = 10^{10}$, $\mathcal{L} = \text{FFT}$, $h(\cdot) = \|\cdot\|_{\ell_1}$, $\vartheta = 1.1$ (HSIs, MRSIs), 1.15 (CIs, CVs), $\varpi = 5 \times 10^{-5}$, $\lambda = \xi / (\max(n_1, n_2) \cdot \prod_{i=3}^d n_i)^{1/2}$, $\xi \in \{1, 1.2, 1.5, 1.8, 2\}$ (CIs),

$\xi \in \{1, 1.2, 1.5, 2, 2.5, 3\}$ (MRSIs), $\xi \in \{1.2, 1.5, 1.8, 2\}$ (HSIs, deterministic algorithm), $\xi \in \{18, 20, 22, 25, 28\}$ (HSIs, randomized algorithms), $\xi \in \{1.2, 1.5, 1.8, 2, 2.2\}$ (CVs, deterministic algorithm), $\xi \in \{2, 4, 6, 8, 10\}$ (CVs, randomized algorithms). For the randomized version using fixed-rank LRTA scheme, we set $\mathbf{q} = [4, 4, *, *]$, $\mathbf{b} = [60, 60, *, *]$ ($SR = 0.1$), $\mathbf{b} = [80, 80, *, *]$ ($SR = 0.2$) in CVs recovery; set $\mathbf{q} = [4, 4, *, *]$, $\mathbf{b} = [80, 80, *, *]$ ($SR = 0.1$), $\mathbf{b} = [100, 100, *, *]$ ($SR = 0.2$) in MRSIs restoration; $\mathbf{q} = [3, 3, *, *]$, $\mathbf{b} = [30, 30, *]$ ($SR = 0.05$), $\mathbf{b} = [40, 40, *]$ ($SR = 0.1$) in HSIs recovery; $\mathbf{q} = [4, 4, *]$, $\mathbf{b} = [300, 300, *]$ in CIs restoration. For the randomized version using fixed-accuracy LRTA scheme, we set $\epsilon = 0.01$, $b = 10$ (HSIs), $b = 40$ (CVs, MRSIs), $b = 100$ (CIs).

2) Results and Analysis of Experiment 3-4: In this part, we set $\mathcal{L} = \text{FFT}$, $\vartheta = 1.15$ (CIs)/1.2 (CVs, MRSIs), $\varpi = 10^{-4}$, $\lambda = \xi / (\max(n_1, n_2) \cdot \prod_{i=3}^d n_i)^{1/2}$, $\xi \in \{1, 1.2, 1.5, 2\}$. Besides, we set $\Phi(\cdot)=\psi(\cdot)=\text{MCP}$, $h(\cdot) = \|\cdot\|_{\ell_1}$, and a specific set of (SR, NR) for simplicity. Figure 11 and Figure 13 present the impact of different fixed-rank and fixed-accuracy LRTA strategies on the restoration performance of the proposed randomized algorithm, respectively. Figure 11 clearly shows that although R-STHOSVD with $q = 0$ can achieve the lowest computational cost in most scenarios, it suffers from the worst estimation accuracy. In comparison to R-STHOSVD with $q = 1$ and $q = 2$, our proposed method demonstrates higher computational efficiency while maintaining similar PSNR values. Overall, for the randomized algorithm induced by R-STHOSVD-BKI strategy, smaller block sizes in Krylov iteration better enhance recovery efficiency. As can be seen from Figure 13, the proposed AD-RSTHOSVD-BLBP scheme demonstrates higher PSNR values over the AD-RSTHOSVD-randQB method (with power parameter $q = 0$) across different block sizes. Especially when dealing with smaller blocks, the proposed method exhibits lower computational complexity compared to the subspace-iteration-based counterpart.

VII. CONCLUSIONS AND FUTURE WORK

In this article, by using several key techniques (i.e., random projection, Krylov-subspace iteration, block Lanczos bidiagonalization process), we first investigate two novel efficient LRTA algorithms under the fixed-precision and fixed-rank paradigms, respectively. Furthermore, we tackle the problem of high-order tensor recovery through generalized non-convex modeling and fast randomized computation strategies. On the theoretical front, we provide error bound analysis and convergence analysis for the proposed approximation and recovery methods. Experiments on a series of large-scale multi-dimensional data have demonstrated the effectiveness and superiority of our proposed algorithms. In the future, we plan to devise novel nonconvex sparse regularization and quantized randomized sketching frameworks for high-order tensors through a model-data dual-driven manner, with the aim of leveraging these tools to explore deep high-order tensor approximation and recovery approaches from the perspective of continuous representation [15], [115].

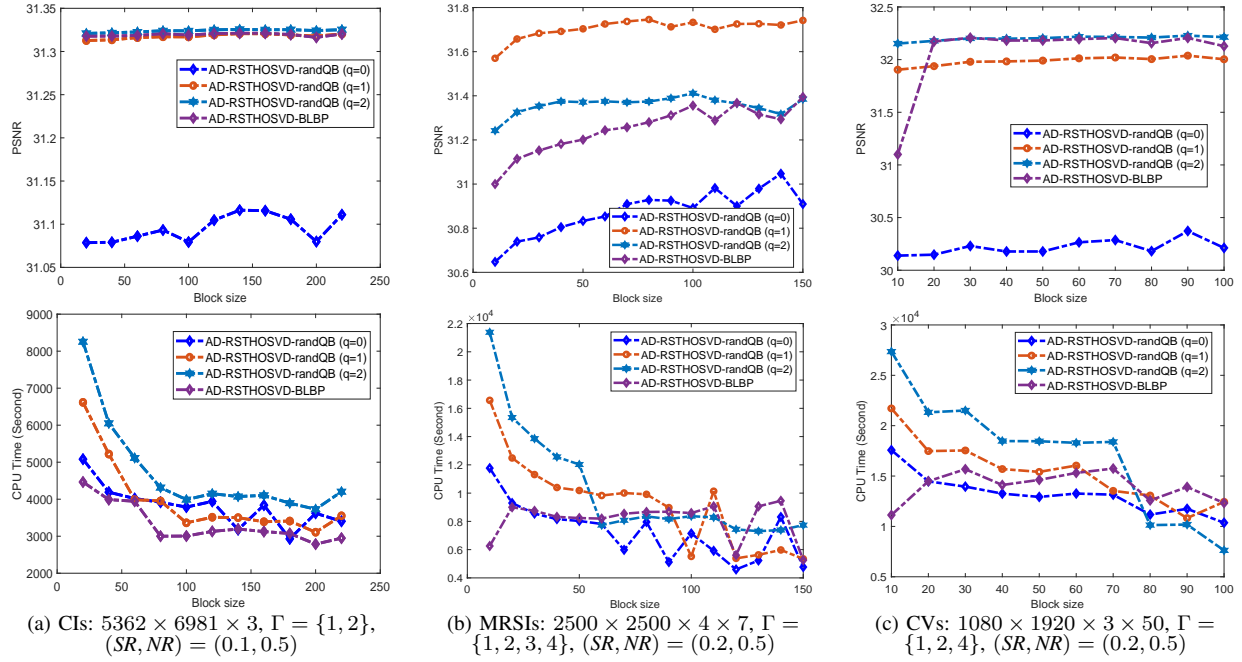


Fig. 13: The influence of various fixed-precision LRTA methods upon restoration performance of the proposed randomized GNRHTC algorithm under different block size b . Each algorithm is run with error tolerance $\epsilon = 0.01$, and the processing order is set to be $\rho = \{1, 2\}$. The remaining modes are not compressed.

REFERENCES

- [1] A. Cichocki, N. Lee, I. Oseledets, A.-H. Phan, Q. Zhao, D. P. Mandic *et al.*, “Tensor networks for dimensionality reduction and large-scale optimization: Part 1 low-rank tensor decompositions,” *Found. Trends Mach. Learn.*, vol. 9, no. 4-5, pp. 249–429, 2016.
- [2] D. Feldman, M. Schmidt, and C. Sohler, “Turning big data into tiny data: Constant-size coresets for k -means, pca, and projective clustering,” *SIAM J. Comput.*, vol. 49, no. 3, pp. 601–657, 2020.
- [3] Y. Liu, *Tensors for data processing: theory, methods, and applications*. Academic Press, 2021.
- [4] Y. Liu, J. Liu, Z. Long, and C. Zhu, *Tensor computation for data analysis*. Springer, 2022.
- [5] R. Han, R. Willett, and A. R. Zhang, “An optimal statistical and computational framework for generalized tensor estimation,” *Ann. Statist.*, vol. 50, no. 1, pp. 1–29, 2022.
- [6] J.-F. Cai, J. Li, and D. Xia, “Generalized low-rank plus sparse tensor estimation by fast Riemannian optimization,” *J. Amer. Statist. Assoc.*, vol. 118, no. 544, pp. 2588–2604, 2023.
- [7] —, “Provable tensor-train format tensor completion by riemannian optimization,” *J. Mach. Learn. Res.*, vol. 23, no. 123, pp. 1–77, 2022.
- [8] T. Tong, C. Ma, A. Prater-Bennette, E. Tripp, and Y. Chi, “Scaling and scalability: Provable nonconvex low-rank tensor estimation from incomplete measurements,” *J. Mach. Learn. Res.*, vol. 23, no. 163, pp. 1–77, 2022.
- [9] Z. Qin, M. B. Wakin, and Z. Zhu, “Guaranteed nonconvex factorization approach for tensor train recovery,” *J. Mach. Learn. Res.*, vol. 25, no. 383, pp. 1–48, 2024.
- [10] C. Lu, J. Feng, Y. Chen, W. Liu, Z. Lin, and S. Yan, “Tensor robust principal component analysis with a new tensor nuclear norm,” *IEEE Trans. Pattern Anal. Mach. Intell.*, vol. 42, no. 4, pp. 925–938, 2019.
- [11] F. Zhang, J. Wang, W. Wang, and C. Xu, “Low-tubal-rank plus sparse tensor recovery with prior subspace information,” *IEEE Trans. Pattern Anal. Mach. Intell.*, vol. 43, no. 10, pp. 3492–3507, 2020.
- [12] J. Hou, F. Zhang, H. Qiu, J. Wang, Y. Wang, and D. Meng, “Robust low-tubal-rank tensor recovery from binary measurements,” *IEEE Trans. Pattern Anal. Mach. Intell.*, vol. 44, no. 8, pp. 4355–4373, 2021.
- [13] J. Wang, J. Hou, and Y. C. Eldar, “Tensor robust principal component analysis from multilevel quantized observations,” *IEEE Trans. Inf. Theory*, vol. 69, no. 1, pp. 383–406, 2022.
- [14] H. Wang, J. Peng, W. Qin, J. Wang, and D. Meng, “Guaranteed tensor recovery fused low-rankness and smoothness,” *IEEE Trans. Pattern Anal. Mach. Intell.*, vol. 45, no. 9, pp. 10990–11007, 2023.
- [15] Y. Luo, X. Zhao, Z. Li, M. K. Ng, and D. Meng, “Low-rank tensor function representation for multi-dimensional data recovery,” *IEEE Trans. Pattern Anal. Mach. Intell.*, vol. 46, no. 5, pp. 3351–3369, 2023.
- [16] W. Qin, H. Wang, F. Zhang, W. Ma, J. Wang, and T. Huang, “Nonconvex robust high-order tensor completion using randomized low-rank approximation,” *IEEE Trans. Image Process.*, vol. 33, pp. 2835–2850, 2024.
- [17] Y. Shi, Y. Gao, Q. Xu, Y. Li, X. Mou, and Z. Liang, “Learned tensor neural network texture prior for photon-counting CT reconstruction,” *IEEE Trans. Med. Imag.*, vol. 43, no. 11, pp. 3830–3842, 2024.
- [18] X. Chen and L. Sun, “Bayesian temporal factorization for multidimensional time series prediction,” *IEEE Trans. Pattern Anal. Mach. Intell.*, vol. 44, no. 9, pp. 4659–4673, 2021.
- [19] R. Zhang, L. Cheng, S. Wang, Y. Lou, Y. Gao, W. Wu, and D. W. K. Ng, “Integrated sensing and communication with massive MIMO: A unified tensor approach for channel and target parameter estimation,” *IEEE Trans. Wireless Commun.*, vol. 23, no. 8, pp. 8571–8587, 2024.
- [20] W. He, Q. Yao, C. Li, N. Yokoya, Q. Zhao, H. Zhang, and L. Zhang, “Non-local meets global: An iterative paradigm for hyperspectral image restoration,” *IEEE Trans. Pattern Anal. Mach. Intell.*, vol. 44, no. 4, pp. 2089–2107, 2020.
- [21] A. Cichocki, D. Mandic, L. De Lathauwer, G. Zhou, Q. Zhao, C. Caiafa, and H. A. Phan, “Tensor decompositions for signal processing applications: From two-way to multiway component analysis,” *IEEE Signal Process. Mag.*, vol. 32, no. 2, pp. 145–163, 2015.
- [22] Y. Panagakis, J. Kossaifi, G. G. Chrysos, J. Oldfield, M. A. Nicolaou, A. Anandkumar, and S. Zafeiriou, “Tensor methods in computer vision and deep learning,” *Proc. IEEE*, vol. 109, no. 5, pp. 863–890, 2021.
- [23] Q. Zhao, L. Zhang, and A. Cichocki, “Bayesian CP factorization of incomplete tensors with automatic rank determination,” *IEEE Trans. Pattern Anal. Mach. Intell.*, vol. 37, no. 9, pp. 1751–1763, 2015.
- [24] Z. Long, C. Zhu, J. Liu *et al.*, “Bayesian low rank tensor ring for image recovery,” *IEEE Trans. Image Process.*, vol. 30, pp. 3568–3580, 2021.
- [25] X.-Y. Liu, S. Aeron, V. Aggarwal, and X. Wang, “Low-tubal-rank tensor completion using alternating minimization,” *IEEE Trans. Inf. Theory*, vol. 66, no. 3, pp. 1714–1737, 2019.
- [26] Y.-B. Zheng, T.-Z. Huang, X.-L. Zhao, Q. Zhao, and T.-X. Jiang, “Fully-connected tensor network decomposition and its application to higher-order tensor completion,” in *Proc. AAAI Conf. Artif. Intel.*, vol. 35, no. 12, 2021, pp. 11071–11078.
- [27] Z.-C. Wu, T.-Z. Huang, L.-J. Deng, H.-X. Dou, and D. Meng, “Tensor wheel decomposition and its tensor completion application,” in *Proc. Adv. Neural Inf. Process. Syst. (NIPS)*, vol. 35, pp. 27008–27020, 2022.

- [28] J. Yu, C. Li, Q. Zhao, and G. Zhao, "Tensor-ring nuclear norm minimization and application for visual: Data completion," in *Proc. IEEE Int. Conf. Acoust., Speech Signal Process. (ICASSP)*. IEEE, 2019, pp. 3142–3146.
- [29] W. Qin, H. Wang, F. Zhang, J. Wang, X. Luo, and T. Huang, "Low-rank high-order tensor completion with applications in visual data," *IEEE Trans. Image Process.*, vol. 31, pp. 2433–2448, 2022.
- [30] Y.-B. Zheng, T.-Z. Huang, X.-L. Zhao, T.-X. Jiang, T.-Y. Ji, and T.-H. Ma, "Tensor n-tubal rank and its convex relaxation for low-rank tensor recovery," *Inf. Sci.*, vol. 532, pp. 170–189, 2020.
- [31] S. Liu, X.-L. Zhao, J. Leng, B.-Z. Li, J.-H. Yang, and X. Chen, "Revisiting high-order tensor singular value decomposition from basic element perspective," *IEEE Trans. Signal Process.*, vol. 72, pp. 4589–4603, 2024.
- [32] L. Feng, C. Zhu, Z. Long, J. Liu, and Y. Liu, "Multiplex transformed tensor decomposition for multidimensional image recovery," *IEEE Trans. Image Process.*, vol. 32, pp. 3397–3412, 2023.
- [33] D. Goldfarb and Z. Qin, "Robust low-rank tensor recovery: Models and algorithms," *SIAM J. Matrix Anal. Appl.*, vol. 35, no. 1, pp. 225–253, 2014.
- [34] H. Huang, Y. Liu, Z. Long, and C. Zhu, "Robust low-rank tensor ring completion," *IEEE Trans. Comput. Imag.*, vol. 6, pp. 1117–1126, 2020.
- [35] X. P. Li, Z.-Y. Wang, Z.-L. Shi, H. C. So, and N. D. Sidiropoulos, "Robust tensor completion via capped frobenius norm," *IEEE Trans. Neural Netw. Learn. Syst.*, vol. 35, no. 7, pp. 9700–9712, 2024.
- [36] Y.-Y. Liu, X.-L. Zhao, G.-J. Song, Y.-B. Zheng, M. K. Ng, and T.-Z. Huang, "Fully-connected tensor network decomposition for robust tensor completion problem," *Inverse Probl. Imag.*, vol. 18, no. 1, pp. 208–238, 2024.
- [37] J. Hou, J. Chen, and M. K. Ng, "Robust tensor completion from uniformly dithered one-bit observations," *SIAM J. Imag. Sci.*, vol. 18, no. 1, pp. 152–215, 2025.
- [38] Q. Jiang and M. Ng, "Robust low-tubal-rank tensor completion via convex optimization," in *Proc. 28th Int. Joint Conf. Artif. Intell.*, 2019, pp. 2649–2655.
- [39] J. Lou and Y.-M. Cheung, "Robust low-rank tensor minimization via a new tensor spectral k -support norm," *IEEE Trans. Image Process.*, vol. 29, pp. 2314–2327, 2019.
- [40] A. Wang, Z. Jin, and G. Tang, "Robust tensor decomposition via t-SVD: Near-optimal statistical guarantee and scalable algorithms," *Signal Process.*, vol. 167, p. 107319, 2020.
- [41] G. Song, M. K. Ng, and X. Zhang, "Robust tensor completion using transformed tensor singular value decomposition," *Numer. Linear Algebr. Appl.*, vol. 27, no. 3, p. e2299, 2020.
- [42] J.-H. Yang, C. Chen, H.-N. Dai, M. Ding, Z.-B. Wu, and Z. Zheng, "Robust corrupted data recovery and clustering via generalized transformed tensor low-rank representation," *IEEE Trans. Neural Netw. Learn. Syst.*, vol. 35, no. 7, pp. 8839–8853, 2024.
- [43] Y. Zhou and Y.-M. Cheung, "Bayesian low-tubal-rank robust tensor factorization with multi-rank determination," *IEEE Trans. Pattern Anal. Mach. Intell.*, vol. 43, no. 1, pp. 62–76, 2019.
- [44] K. Gao and Z.-H. Huang, "Tensor robust principal component analysis via tensor fibered rank and ℓ_p minimization," *SIAM J. Imaging Sci.*, vol. 16, no. 1, pp. 423–460, 2023.
- [45] Q. Yu and M. Bai, "Generalized nonconvex hyperspectral anomaly detection via background representation learning with dictionary constraint," *SIAM J. Imag. Sci.*, vol. 17, no. 2, pp. 917–950, 2024.
- [46] W. Qin, H. Wang, F. Zhang, J. Wang, X. Cao, and X.-L. Zhao, "Tensor ring decomposition-based generalized and efficient nonconvex approach for hyperspectral anomaly detection," *IEEE Trans. Geosci. Remote Sens.*, vol. 62, 2024, Art. no. 5539818.
- [47] X. Liu, J. Hou, J. Peng, H. Wang, D. Meng, and J. Wang, "Tensor compressive sensing fused low-rankness and local-smoothness," in *Proc. AAAI Conf. Artif. Intell.*, vol. 37, no. 7, 2023, pp. 8879–8887.
- [48] J. Hou, X. Liu, H. Wang, and K. Guo, "Tensor recovery from binary measurements fused low-rankness and smoothness," *Signal Process.*, vol. 221, p. 109480, 2024.
- [49] Z. Liu, Z. Han, Y. Tang, X.-L. Zhao, and Y. Wang, "Low-tubal-rank tensor recovery via factorized gradient descent," *IEEE Trans. Signal Process.*, vol. 72, pp. 5470–5483, 2024.
- [50] H. Wang, F. Zhang, J. Wang, T. Huang, J. Huang, and X. Liu, "Generalized nonconvex approach for low-tubal-rank tensor recovery," *IEEE Trans. Neural Netw. Learn. Syst.*, vol. 33, no. 8, pp. 3305–3319, 2021.
- [51] M. Yang, Q. Luo, W. Li, and M. Xiao, "3-D array image data completion by tensor decomposition and nonconvex regularization approach," *IEEE Trans. Signal Process.*, vol. 70, pp. 4291–4304, 2022.
- [52] Z.-Y. Wang, H. C. So, and A. M. Zoubir, "Low-rank tensor completion via novel sparsity-inducing regularizers," *IEEE Trans. Signal Process.*, vol. 72, pp. 3519–3534, 2024.
- [53] H. Zhang, X. Liu, C. Liu, H. Fan, Y. Li, and X. Zhu, "Tensor recovery based on a novel non-convex function minimax logarithmic concave penalty function," *IEEE Trans. Image Process.*, vol. 32, pp. 3413–3428, 2023.
- [54] L. Chen, X. Jiang, X. Liu, and Z. Zhou, "Robust low-rank tensor recovery via nonconvex singular value minimization," *IEEE Trans. Image Process.*, vol. 29, pp. 9044–9059, 2020.
- [55] D. Qiu, M. Bai *et al.*, "Nonlocal robust tensor recovery with nonconvex regularization," *Inverse Probl.*, vol. 37, no. 3, p. 035001, 2021.
- [56] X. Zhao, M. Bai, D. Sun, and L. Zheng, "Robust tensor completion: Equivalent surrogates, error bounds, and algorithms," *SIAM J. Imaging Sci.*, vol. 15, no. 2, pp. 625–669, 2022.
- [57] D. Qiu, B. Yang, and X. Zhang, "Robust tensor completion via dictionary learning and generalized nonconvex regularization for visual data recovery," *IEEE Trans. Circuits Syst. Video Technol.*, 2024.
- [58] W. Qin, H. Wang, F. Zhang, M. Dai, and J. Wang, "Robust low-rank tensor reconstruction using high-order t-SVD," *J. Electron. Imag.*, vol. 30, no. 6, pp. 063 016–063 016, 2021.
- [59] W. Qin, H. Wang, W. Ma, and J. Wang, "Robust high-order tensor recovery via nonconvex low-rank approximation," in *Proc. IEEE Int. Conf. Acoust., Speech Signal Process. (ICASSP)*, 2022, pp. 3633–3637.
- [60] N. Halko, P.-G. Martinsson, and J. A. Tropp, "Finding structure with randomness: Probabilistic algorithms for constructing approximate matrix decompositions," *SIAM Rev.*, vol. 53, no. 2, pp. 217–288, 2011.
- [61] P.-G. Martinsson and J. A. Tropp, "Randomized numerical linear algebra: Foundations and algorithms," *Acta Numer.*, vol. 29, pp. 403–572, 2020.
- [62] P.-G. Martinsson and S. Voronin, "A randomized blocked algorithm for efficiently computing rank-revealing factorizations of matrices," *SIAM J. Sci. Comput.*, vol. 38, no. 5, pp. S485–S507, 2016.
- [63] J. A. Tropp, A. Yurtsever, M. Udell, and V. Cevher, "Practical sketching algorithms for low-rank matrix approximation," *SIAM J. Matrix Anal. Appl.*, vol. 38, no. 4, pp. 1454–1485, 2017.
- [64] W. Yu, Y. Gu, and Y. Li, "Efficient randomized algorithms for the fixed-precision low-rank matrix approximation," *SIAM J. Matrix Anal. Appl.*, vol. 39, no. 3, pp. 1339–1359, 2018.
- [65] J. A. Duersch and M. Gu, "Randomized projection for rank-revealing matrix factorizations and low-rank approximations," *SIAM Rev.*, vol. 62, no. 3, pp. 661–682, 2020.
- [66] E. Hallman, "A block bidiagonalization method for fixed-accuracy low-rank matrix approximation," *SIAM J. Matrix Anal. Appl.*, vol. 43, no. 2, pp. 661–680, 2022.
- [67] J. Demmel, L. Grigori, and A. Rusciano, "An improved analysis and unified perspective on deterministic and randomized low-rank matrix approximation," *SIAM J. Matrix Anal. Appl.*, vol. 44, no. 2, pp. 559–591, 2023.
- [68] J. A. Tropp and R. J. Webber, "Randomized algorithms for low-rank matrix approximation: Design, analysis, and applications," *arXiv preprint arXiv:2306.12418*, 2023.
- [69] X. Fu, S. Ibrahim, H.-T. Wai, C. Gao, and K. Huang, "Block-randomized stochastic proximal gradient for low-rank tensor factorization," *IEEE Trans. Signal Process.*, vol. 68, pp. 2170–2185, 2020.
- [70] B. W. Larsen and T. G. Kolda, "Practical leverage-based sampling for low-rank tensor decomposition," *SIAM J. Matrix Anal. Appl.*, vol. 43, no. 3, pp. 1488–1517, 2022.
- [71] F. Zhang, L. Yang, J. Wang, and X. Luo, "Randomized sampling techniques based low-tubal-rank plus sparse tensor recovery," *Knowl.-Based Syst.*, vol. 261, p. 110198, 2023.
- [72] D. A. Tarzanagh *et al.*, "Fast randomized algorithms for t-product based tensor operations and decompositions with applications to imaging data," *SIAM J. Imaging Sci.*, vol. 11, no. 4, pp. 2629–2664, 2018.
- [73] J. Zhang, A. K. Saibaba, M. E. Kilmer, and S. Aeron, "A randomized tensor singular value decomposition based on the t-product," *Numer. Linear Algebr. Appl.*, vol. 25, no. 5, p. e2179, 2018.
- [74] M. Che, X. Wang, Y. Wei, and X. Zhao, "Fast randomized tensor singular value thresholding for low-rank tensor optimization," *Numer. Linear Algebr. Appl.*, vol. 29, no. 6, p. e2444, 2022.
- [75] M. Che, Y. Wei, and H. Yan, "The computation of low multilinear rank approximations of tensors via power scheme and random projection," *SIAM J. Matrix Anal. Appl.*, vol. 41, no. 2, pp. 605–636, 2020.
- [76] —, "Randomized algorithms for the low multilinear rank approximations of tensors," *J. Comput. Appl. Math.*, vol. 390, p. 113380, 2021.

- [77] —, “An efficient randomized algorithm for computing the approximate tucker decomposition,” *J. Sci. Comput.*, vol. 88, no. 2, p. 32, 2021.
- [78] M. Che, Y. Wei, and Y. Xu, “Randomized algorithms for the computation of multilinear rank- (μ_1, μ_2, μ_3) approximations,” *J. Global Optim.*, vol. 87, no. 2, pp. 373–403, 2023.
- [79] W. Dong, G. Yu, L. Qi, and X. Cai, “Practical sketching algorithms for low-rank tucker approximation of large tensors,” *J. Sci. Comput.*, vol. 95, no. 2, p. 52, 2023.
- [80] R. Chhaya, J. Choudhari, A. Dasgupta, and S. Shit, “Streaming coresets for symmetric tensor factorization,” in *Proc. Int. Conf. Mach. Learn. (ICML)*, 2020, pp. 1855–1865.
- [81] T. G. Kolda and B. W. Bader, “Tensor decompositions and applications,” *SIAM Rev.*, vol. 51, no. 3, pp. 455–500, 2009.
- [82] C. D. Martin, R. Shafer, and B. LaRue, “An order- p tensor factorization with applications in imaging,” *SIAM J. Sci. Comput.*, vol. 35, no. 1, pp. A474–A490, 2013.
- [83] J. Chen, C.-L. Wang, M. K. Ng, and D. Wang, “High dimensional statistical estimation under uniformly dithered one-bit quantization,” *IEEE Trans. Inf. Theory*, vol. 69, no. 8, pp. 5151–5187, 2023.
- [84] N. Vannieuwenhoven, R. Vandebril, and K. Meerbergen, “A new truncation strategy for the higher-order singular value decomposition,” *SIAM J. Sci. Comput.*, vol. 34, no. 2, pp. A1027–A1052, 2012.
- [85] R. Minster, A. K. Saibaba, and M. E. Kilmer, “Randomized algorithms for low-rank tensor decompositions in the tucker format,” *SIAM J. Math. Data Sci.*, vol. 2, no. 1, pp. 189–215, 2020.
- [86] C. Musco and C. Musco, “Randomized block krylov methods for stronger and faster approximate singular value decomposition,” *Proc. Adv. Neural Inf. Process. Syst. (NIPS)*, vol. 28, 2015.
- [87] Q. Yuan, M. Gu, and B. Li, “Superlinear convergence of randomized block Lanczos algorithm,” in *Proc. IEEE Int. Conf. Data Mining (ICDM)*. IEEE, 2018, pp. 1404–1409.
- [88] R. Meyer, C. Musco, and C. Musco, “On the unreasonable effectiveness of single vector krylov methods for low-rank approximation,” in *Proc. Annu. ACM-SIAM Symp. Discrete Algorithms (SODA)*, 2024, pp. 811–845.
- [89] Y. Chen, S. Wang, and Y. Zhou, “Tensor nuclear norm-based low-rank approximation with total variation regularization,” *IEEE J. Sel. Topics Signal Process.*, vol. 12, no. 6, pp. 1364–1377, 2018.
- [90] D. Qiu, M. Bai, M. K. Ng, and X. Zhang, “Robust low-rank tensor completion via transformed tensor nuclear norm with total variation regularization,” *Neurocomputing*, vol. 435, pp. 197–215, 2021.
- [91] H.-Y. Gao and A. G. Bruce, “Waveshrink with firm shrinkage,” *Statistica Sinica*, pp. 855–874, 1997.
- [92] P. Gong, C. Zhang, Z. Lu, J. Huang, and J. Ye, “A general iterative shrinkage and thresholding algorithm for non-convex regularized optimization problems,” in *Proc. Int. Conf. Mach. Learn. (ICML)*. PMLR, 2013, pp. 37–45.
- [93] G. Marjanovic and V. Solo, “On ℓ_q optimization and matrix completion,” *IEEE Trans. signal process.*, vol. 60, no. 11, pp. 5714–5724, 2012.
- [94] J. Fan and R. Li, “Variable selection via nonconcave penalized likelihood and its oracle properties,” *J. Amer. Statist. Assoc.*, vol. 96, no. 456, pp. 1348–1360, 2001.
- [95] C.-H. Zhang, “Nearly unbiased variable selection under minimax concave penalty,” *Ann. Statist.*, vol. 38, no. 2, pp. 894–942, 2010.
- [96] G. Li, G. Guo, S. Peng, C. Wang, S. Yu, J. Niu, and J. Mo, “Matrix completion via Schatten capped p norm,” *IEEE Trans. Knowl. Data Eng.*, vol. 34, no. 1, pp. 394–404, 2020.
- [97] L. Pan and X. Chen, “Group sparse optimization for images recovery using capped folded concave functions,” *SIAM J. Imag. Sci.*, vol. 14, no. 1, pp. 1–25, 2021.
- [98] M. K. Ng, X. Zhang *et al.*, “Patched-tube unitary transform for robust tensor completion,” *Pattern Recognit.*, vol. 100, p. 107181, 2020.
- [99] X. Zhao, M. Bai, and M. K. Ng, “Nonconvex optimization for robust tensor completion from grossly sparse observations,” *J. Sci. Comput.*, vol. 85, no. 2, p. 46, 2020.
- [100] Z. Zhang, S. Liu, and Z. Lin, “A generalized non-convex method for robust tensor completion,” *J. Sci. Comput.*, vol. 96, no. 3, p. 91, 2023.
- [101] A. Wang, X. Song, X. Wu, Z. Lai, and Z. Jin, “Robust low-tubal-rank tensor completion,” in *Proc. IEEE Int. Conf. Acoust., Speech Signal Process. (ICASSP)*, 2019, pp. 3432–3436.
- [102] F. Zhang, H. Wang, W. Qin, X. Zhao, and J. Wang, “Generalized nonconvex regularization for tensor RPCA and its applications in visual inpainting,” *Appl. Intell.*, vol. 53, no. 20, pp. 23 124–23 146, 2023.
- [103] F. Nie, H. Wang, H. Huang, and C. Ding, “Joint Schatten p -norm and ℓ_p -norm robust matrix completion for missing value recovery,” *Knowl. Inf. Syst.*, vol. 42, no. 3, pp. 525–544, 2015.
- [104] C. Lu, J. Tang, S. Yan, and Z. Lin, “Nonconvex nonsmooth low rank minimization via iteratively reweighted nuclear norm,” *IEEE Trans. Image Process.*, vol. 25, no. 2, pp. 829–839, 2015.
- [105] Q. Yao, J. T. Kwok, T. Wang, and T.-Y. Liu, “Large-scale low-rank matrix learning with nonconvex regularizers,” *IEEE Trans. Pattern Anal. Mach. Intell.*, vol. 41, no. 11, pp. 2628–2643, 2018.
- [106] F. Wen, R. Ying, P. Liu, and R. C. Qiu, “Robust PCA using generalized nonconvex regularization,” *IEEE Trans. Circuits Syst. Video Technol.*, vol. 30, no. 6, pp. 1497–1510, 2019.
- [107] H. Zhang, F. Qian, P. Shi, W. Du, Y. Tang, J. Qian, C. Gong, and J. Yang, “Generalized nonconvex nonsmooth low-rank matrix recovery framework with feasible algorithm designs and convergence analysis,” *IEEE Trans. Neural Netw. Learn. Syst.*, vol. 34, no. 9, pp. 5342–5353, 2022.
- [108] Z. Wang, D. Hu, Z. Liu, C. Gao, and Z. Wang, “Iteratively capped reweighting norm minimization with global convergence guarantee for low-rank matrix learning,” *IEEE Trans. Pattern Anal. Mach. Intell.*, vol. 47, no. 3, pp. 1923–1940, 2025.
- [109] S. Boyd, N. Parikh, E. Chu *et al.*, “Distributed optimization and statistical learning via the alternating direction method of multipliers,” *Found. Trends Mach. Learn.*, vol. 3, no. 1, pp. 1–122, 2011.
- [110] Y. Wang, J. Yang, W. Yin, and Y. Zhang, “A new alternating minimization algorithm for total variation image reconstruction,” *SIAM J. Imaging Sci.*, vol. 1, no. 3, pp. 248–272, 2008.
- [111] J. Hou, F. Zhang, and J. Wang, “One-bit tensor completion via transformed tensor singular value decomposition,” *Appl. Math. Model.*, vol. 95, pp. 760–782, 2021.
- [112] N. Ghadermarzy, Y. Plan, and O. Yilmaz, “Learning tensors from partial binary measurements,” *IEEE Trans. Signal Process.*, vol. 67, no. 1, pp. 29–40, 2019.
- [113] A. Aidini, G. Tsagkarakis, and P. Tsakalides, “1-bit tensor completion,” *Electronic Imaging*, vol. 30, pp. 1–6, 2018.
- [114] M. A. Davenport, Y. Plan, E. Van Den Berg, and M. Wootters, “1-bit matrix completion,” *Inf. Inference*, vol. 3, no. 3, pp. 189–223, 2014.
- [115] Y. Luo, X. Zhao, and D. Meng, “Revisiting nonlocal self-similarity from continuous representation,” *IEEE Trans. Pattern Anal. Mach. Intell.*, vol. 47, no. 1, pp. 450–468, 2025.